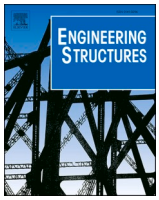
Engineering Structures 301 (2024) 117289



Contents lists available at ScienceDirect

Engineering Structures

journal homepage: www.elsevier.com/locate/engstruct





Fluid-structure interaction analysis of wind turbine aerodynamic loads and aeroelastic responses considering blade and tower flexibility

Dongqin Zhang [a], Zhenqing Liu [b,*], Weipeng Li [b], Jize Zhang [c], Ling Cheng [d], Gang Hu [a]

[a] School of Civil and Environmental Engineering, Harbin Institute of Technology, Shenzhen 518055, China
[b] School of Civil and Hydraulic Engineering, Huazhong University of Science and Technology, Wuhan, Hubei 430074, China
[c] Department of Civil and Environmental Engineering, The Hong Kong University of Science and Technology, Hong Kong, China
[d] School of Electrical and Information Engineering, University of the Witwatersrand, Johannesburg 2000, South Africa

ARTICLE INFO

Keywords:
Fluid-structure interaction
Large eddy simulation
Aerodynamic loads
Aeroelastic response
Wind turbine

ABSTRACT

With the increasing size of wind turbines, the aeroelastic phenomenon plays an essential role in the safety of wind turbines. A fluid-structure interaction (FSI) analysis for wind turbine by integrating the LES turbulent model and a structural dynamic model is carried out to investigate the aerodynamic loads and aeroelastic responses considering different inflow conditions, and blade and tower flexibility. For the first time, the time series and statistical features of aerodynamic loads, the exceedance probability, the equivalent fatigue loads, and the time series and statistical features of aeroelastic responses of wind turbine are calculated by the two-way FSI model. Furthermore, effects of inflow wind conditions and the blade and tower flexibility are investigated. It is noted that the turbulent winds result in increased fluctuations of aerodynamic loads and the equivalent fatigue load. The flap-wise motions of blades are more critical to load magnitude than the edgewise motions, and the inclusion of tower motion mitigates this aerodynamic load due to the coupling effects. Finally, it is also observed that the tower motion has a noticeable impact on the flap-wise displacement at the blade tip, and the flap-wise motions of blades significantly affect the fore-aft displacement at the tower top.

1. Introduction

As modern society continues to advance, there is a mounting global demand for energy. However, traditional energy sources such as fossil fuels have resulted in significant environmental pollution and climate change. As a result, there is an urgent need to develop renewable energy sources, which are the most effective means of reducing fossil fuel consumption and carbon emissions. Among the various renewable energy sources available today, wind energy shows great promise. According to the World Wind Energy Association (WWEA) [1], the installed wind turbine capacity all over the world has been on a continuous upward trajectory over the past two decades. In 2021 alone, the wind power market added 97.3 GW of capacity, setting a new record for annual added capacity.

Recently, wind turbines have been designed with larger swept areas and higher towers to increase power generation capacity and to improve the effectiveness of wind energy utilization. Over time, there have been significant advancements in turbine technology, with modern turbines boasting diameters of up to 242 m and power outputs reaching as high as 16 MW. In addition, hub heights have risen dramatically, with current heights exceeding 100 m and projected to continue increasing. However, as turbines have become larger, the blades and tower have become more flexible [2], leading to considerable aeroelastic deformation during operation, which can severely diminish power generation efficiency and lifespan, negatively impacting overall performance or even causing accidents, such as the turbine collapse that occurred in Gansu province, China in 2019, as shown in Fig. 1. Therefore, accurate assessment of wind turbine aerodynamics and aeroelastics is essential.

Three commonly methods to evaluate turbine aerodynamics are blade element momentum (BEM) theory, computational fluid dynamics (CFD) simulation, and experiments. BEM theory method [3] is based on the fundamental assumptions of quasi-steady flows and two-dimensional aerodynamics. Although BEM theory is computationally efficient and yields reasonable results, it cannot accurately simulate the vortices generated by blades and fails to consider large blade deflection, as it neglects the radial flow component. To address these issues, various corrections such as Prandtl's tip loss model [4], the dynamic stall model [5,6], and the Glauert's model [7] have been proposed

* Corresponding author.
E-mail address: liuzhenqing@hust.edu.cn (Z. Liu).

https://doi.org/10.1016/j.engstruct.2023.117289
Received 24 May 2023; Received in revised form 21 October 2023; Accepted 3 December 2023
Available online 16 December 2023
0141-0296/© 2023 Elsevier Ltd. All rights reserved.



Fig. 1. Wind turbine collapse accidents in Gansu province, China.

to describe the realistic flow dynamics of blades. Additionally, improved versions of BEM theory have been used, including wake rotation and radial flow improved BEM theory [8] and low tip speed ratio wind turbines improved BEM theory [9]. In the pursuit of accurately evaluating the aerodynamic loads on wind turbine blades, several methods have been developed, including the utilization of CFD simulations and wind tunnel testing. CFD simulations are able to capture the flow fields around the blades in detail and provide accurate information on velocity, pressure, and turbulence distributions [10]. Typically, the blades are placed in a rotating region and the information of the flow fields is transferred to the surrounding fixed region using the dynamic mesh technique [11,12]. Although CFD simulations are more accurate compared to BEM theory, they require more computational resources and are time-consuming. Wind tunnel testing, on the other hand, involves the use of scale models of wind turbines with specific inflow condition to obtain accurate and stable results, but this method is expensive [13,14].

To assess the aeroelastic responses of wind turbines, the turbine blade is modelled using either the 3D finite element method (FEM) or 1D beam element. Although the three-dimensional FEM can be used to evaluate the stress distribution within a blade, it is computationally expensive, thus limiting its widespread application in FSI analysis for wind turbine. Conversely, the 1D beam element requires less computational resources than the 3D FEM and can provide acceptable results [15]. There are three common approaches to discretize the blade into various 1D beam element: 1D FEM, multi-body dynamics (MBD), and modal approach [16]. In the 1D FEM, an approximate solution is obtained by analyzing a series of finite elements that are connected by nodes. MBD is another approach that connects rigid bodies using springs and dampers to evaluate the aeroelastic responses of a wind turbine. Lastly, the modal approach is the simplest one where the blade deflection shape is calculated by the sum of several mode shape functions.

To account for the blade flexibility effects in wind turbines, FSI analysis is commonly conducted, with one-way and two-way FSI being the two adopted approaches [17]. One-way FSI analysis determines the aeroelastic responses of wind turbines using computational structural dynamics (CSD) after the evaluation of aerodynamic loads. Open-source programs and commercial software generally adopt the BEM theory to calculate aerodynamic loads, and use different methods to calculate the aeroelastic responses of wind turbines [18]. Programs such as ADAMS/WT [19], SIMPACK/Wind [20], and PHATAS [21] combine BEM and MBD to carry out FSI analysis, whereas FLEX5 [22] and BH Bladed [23] utilize both the modal approach and FEM, and HAWC2 [24] and BHawC [25] utilize MBD and FEM. OpenFAST [26] can use either the modal approach or MBD to conduct FSI analysis. In contrast, the two-way FSI analysis considers the coupling effects between blade motions and aerodynamic loads. It involves the initial calculation of aerodynamic loads on blades, which are then substituted into the finite element structural model. Any deflection of the blades is subsequently imported into the CFD program for further analysis. This coupled analysis continues until the convergence criterion is achieved. The efficacy of this approach is demonstrated through several studies by different research groups. Carrión et al. [27] used the coupled CFD-CSD model to investigate the aerodynamic loads on the NREL Annex XX blade and found that the torque elastic blades increased by 13% due to rapid blade oscillation compared to rigid blades. Similarly, Yu and Kwon [28] used the coupled method to investigate the aerodynamic loads and aeroelastic deflections of blades and observed a significant decrease in aerodynamic loads due to blade deflection. On the other hand, Della Posta et al. [29] found that one-way FSI analysis overpredicts aeroelastic responses. Dose et al. [30] also noted that rigid CFD solvers underpredict aerodynamic loads on blades compared to FSI analysis. Sayed et al. [31] proposed a CFD-CSD coupling model to investigate aeroelastic deformation of a DTU 10 MW wind turbine and found that thrust forces on blades and towers increase due to the impact of blade radial force. Chen et al. [32] proposed a complex-valued modal model to study the structural responses of wind turbine and proved that it is an effective method. The findings of these studies highlight the importance of a two-way FSI analysis to accurately predict the aeroelastic performance of blades.

The aerodynamic loads and aeroelastic responses of wind turbine are also influenced by the inflow conditions. Previous studies have utilized a two-way FSI model, examining both uniform and turbulent inflow conditions [33–35] and under turbulent inflow condition [12,36]. Specifically, Sabale and Gopal [36] conducted a study on the aeroelastic response of wind turbines in stochastically turbulent winds, analyzing the impact of turbulence components. Zhou et al. [37] explored the effect of inflow wind conditions on the aerodynamics and aeroelastics of a floating wind turbine, discovering that turbulence increases fluctuations in thrust force and power. In addition, Li et al. [38] investigated the correlation between turbulent intensity and power performance and, finally, Li et al. [39] examined the effect of unsteady periodic inflows on the aerodynamics of flexible blades. Despite these studies, there remains a need for systematic investigation into the impact of inflow conditions on the aerodynamic loads and aeroelastic response of wind turbines.

Prior research has highlighted the significance of this interaction in this context. However, there are still several research gaps that need to be filled:

- There are discrepancies in the two-way FSI models proposed by researchers, and the impact of blade and tower flexibility have not been discussed.
- Existing studies have mostly focused on calculating the mean aerodynamic loads, while neglecting to explore other important factors, such as the time-historical, the statistical features, and the exceedance probability of aerodynamic loads, and the equivalent fatigue loads.
- The statistical properties of aeroelastic response of the blades and tower remain unexplored.

Table 1
Blade section parameters of a 4.5WM wind turbine.

No.	Section radius (m)	Relative thickness (%)	Twist angle (°)	Chord length (m)	Airfoil
1	0	100	9.50	2.90	Cylinder
2	1	100	9.50	2.90	Cylinder
3	9.22	60	10.91	4.22	TR25–2d
4	16.67	40	8.57	4.64	DU00-W2–401
5	23.82	35	6.60	4.09	DU00-W2–350
6	39.62	30	1.60	2.43	DU97-W-300
7	59.84	25	-1.02	1.29	DU91W2–250
8	69.04	21	-2.04	0.94	NACA-63421
9	72	18.00	-2.50	0.80	NACA-63618

- The effects of inflow wind conditions, including uniform and turbulent winds on aerodynamic loads and aeroelastic responses of wind turbine have not been systematically examined.

To address the aforementioned gaps in the literature, this study proposes a high-fidelity two-way FSI model that integrates distinct blade and tower flexibility, and varying inflow conditions, to rigorously analyze the aerodynamic loads and aeroelastic responses of wind turbines. The paper is organized as follows: Section 2 provides detailed information on the CFD simulations. Section 3 presents the FSI model. The case setting, aerodynamic loads and aeroelastic responses of wind turbine are calculated considering blades and tower flexibility, and inflow conditions in Section 4. Conclusions are summarized in Section 5.

2. CFD simulations

2.1. Governing equations

Large eddy simulation (LES) has become the preferred numerical method for investigating the aerodynamic properties of wind turbines due to its exceptional accuracy in handling the non-linear and turbulent effects in fluid flow. The LES technique partitions turbulent flow into two constituents: larger vortices that are directly simulated and smaller vortices that are modelled. In consideration of the high Reynolds number that is characteristic of the flow field, simulating turbulence with precision is imperative. Consequently, the LES turbulence model is an indispensable tool in this study.

The governing equations, i.e., continuity and momentum conservation equations, obtained by filtering the time-dependent Navier-Stokes equations are expressed as follows:

$$\frac{\partial \rho \widetilde{u_i}}{\partial x_i} = 0 \tag{1}$$

$$\frac{\partial \rho \widetilde{u_i}}{\partial t} + \partial \rho \frac{\widetilde{u_i}\widetilde{u_j}}{\partial x_j} = \frac{\partial}{\partial x_j}\left(\mu \frac{\partial \widetilde{u_i}}{\partial x_j}\right) - \frac{\partial \widetilde{p}}{\partial x_i} - \frac{\partial \tau_{ij}}{\partial x_j} \tag{2}$$

where $\widetilde{u_i}$ $(i = 1, 2.3)$ and $\widetilde{p}$ are the filtered velocities and pressure, respectively, ρ refers to air density and it is equal to $1.225 kg/m^3$, μ shows the viscosity, τ_{ij} represents the subgrid-scale (SGS) stress.

It is obvious that the above governing equations are not closed and the anisotropic residual stress tensor τ_{ij} is modelled as:

$$\tau_{ij} = -2\mu_t \widetilde{S}_{ij} + \frac{1}{3}\tau_{kk}\delta_{ij} \tag{3}$$

$$\widetilde{S}_{ij} = \frac{1}{2}\left(\frac{\partial \widetilde{u_i}}{\partial x_j} + \frac{\partial \widetilde{u_j}}{\partial x_i}\right) \tag{4}$$

where μ_t is the SGS turbulent viscosity, $\widetilde{S}_{ij}$ represents the rate-of-strain tensor for the resolved scale, δ_{ij} shows the Kronecker delta.

The standard Smagorinsky-Lilly model is employed for the SGS turbulent viscosity μ_t which can be expressed as follows:

$$\mu_t = \rho L_s^2 \left|\widetilde{S}\right| = \rho L_s^2 \sqrt{2\widetilde{S}_{ij}\widetilde{S}_{ij}}, L_s = \min\left(\kappa d, C_s \Lambda^{1/3}\right) \tag{5}$$

where L_s shows the SGS mixing length, κ is the von Kármán constant which is equal to 0.42, d stands for the distance to the closest wall, C_s denotes the Smagorinsky constant with a value of 0.01.

2.2. Computational domain and inflow boundary condition

For the FSI analysis, a 4.5 MW wind turbine is selected where a blade with seven distinct airfoil types is modelled. Table 1 outlines the various blade parameters, such as section radius, relative thickness, twist angle, chord length, and airfoil type. The blade sections are designed using different airfoils, including the cylinder, DU, NACA, and TR25–2d airfoils, with the TR25–2d airfoil used for the transition between the root and middle sections due to its high relative thickness. The relative thickness decreases from 40% to 25% at 5% intervals in the middle section by utilizing four DU airfoils, and from 21% to 18% in the tip section with two NACA airfoils. The seven airfoil types selected for the blade sections are TR25–2d, DU00-W2–401, DU00-W2–350, DU97-W-300, DU91W2–250, NACA-63421, and NACA-63618. The blade length is 76 m, and the linear interpolation method is used for transition sections between different airfoils to obtain 16 cross-sections.

In wind turbine systems, the blade operates within the rotation domain, while the nacelle and tower are situated in the dynamic domain. As a result, the hub and nacelle of a 4.5 MW wind turbine are not physically connected. Although there may be some impact on the flow field behind the hub, this effect is considered negligible. Detailed specifications for the aforementioned wind turbine are presented in Table 2, highlighting its key parameters.

Fig. 2 illustrates the computational domain with dimensions of 1700 m in length, 456 m in width, and 398 m in height. The wind turbine is positioned 500 m from the inlet, with a refined wake region spanning 300 m. The dynamic domain is a cuboid with dimensions of 100 m in length, 240 m in width, and 188 m in height, where the rotation domain is situated in the central part. The rotation domain has a diameter of 170 m with 5 m extensions at the front and back, resulting in a thickness of 10 m. The tower has a height of 94 m. The computational domain is characterized by symmetrical surfaces on the side and top, with a wall surface on the bottom. The inlet is designated as a velocity inlet, while the outlet is a pressure outlet. Table 3 presents the specific boundary conditions utilized in the simulation.

The atmospheric boundary layer (ABL) flow can be generated by CFD simulations, based on experiments conducted by Ishihara et al. [40]. As shown in Fig. 3, the computational domain has dimensions of 15.5 m in length, 1.5 m in width, and 1.8 m in height. The turbulent wind has fully developed, and the extraction plane is located 3.5 m from the spire, which is utilized as a velocity inlet of the wind turbine computational

Table 2
Key parameters of a 4.5 MW wind turbine.

Rated power	Rated speed	Rotor diameter	Number of blades	Elevation and cone angles	Hub diameter	Hub height	Tower top diameter	Tower bottom diameter
4.5 MW	10 rpm	152 m	3	0° , 0°	5 m	94 m	4 m	4.5 m

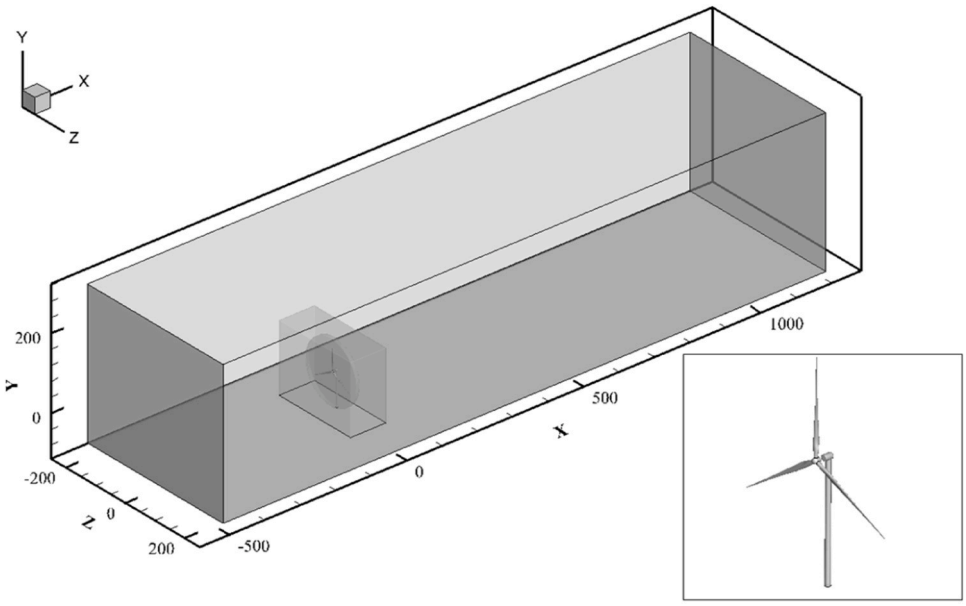


Fig. 2. Configurations of the computational domain wind boundary conditions.

Table 3
Boundary conditions for the computational domain.

Position	Boundary type	Physical meaning
Inlet of the domain	Velocity inlet	$\tilde{u} = \frac{10\ m}{s}, \partial\tilde{v}/\partial n = 0, \partial\tilde{w}/\partial n = 0, \partial\tilde{p}/\partial n = 0$
Outlet of the domain	Pressure-outlet	$\tilde{p} = 0, \partial\tilde{u}_i/\partial n = 0$
Top of the domain	Symmetry	$\partial\tilde{u}/\partial n = 0, \partial\tilde{v}/\partial n = 0, \tilde{w} = 0, \partial\tilde{p}/\partial n = 0$
Lateral sides of the domain	Symmetry	$\partial\tilde{u}/\partial n = 0, \partial\tilde{w}/\partial n = 0, \tilde{v} = 0, \partial\tilde{p}/\partial n = 0$
Spire and ground	Non-slip wall	$\partial\tilde{p}/\partial n = 0, \tilde{u}_i = 0$

domain. The computational domain employs the structured grid with a minimum mesh size of 2 mm and 1 mm in the horizontal and vertical directions, resulting in a total of 7.2 million grids. The incoming flow is uniform. The bottom of the computational domain and the spire utilize wall boundary conditions, while the side and top surfaces employ symmetry boundary conditions. The outlet is a pressure outlet, consistent with the boundary conditions of wind turbine computational domain.

The instantaneous turbulent wind extracted at the extraction plane is displayed in Fig. 3. To visualize the turbulent wind, the vertical profiles of the mean wind speed and turbulence intensity are presented in Fig. 4.

The extraction surface is partitioned into 20 × 20 grids, resulting in 400 points, from which the velocity time history is extracted. A time step of 0.01 s is employed, and the calculation is executed for a total of 20000 time steps, corresponding to 200 s. The data for the last 10,000 time steps or 100 s, is then utilized as the inlet velocity for the wind turbine computational domain, presented in Fig. 2. Accurately capturing the turbulent wind data is crucial in simulating the flow behavior and obtaining reliable results. The extracted velocity time history from the extraction plane is adopted as the inlet velocity in the wind turbine computational domain, which is a commonly employed practice in wind energy research.

2.3. Numerical grids

Fig. 4 illustrates the numerical grids adopted with a total number of about 7.2 million. The turbine blades are placed in the rotation domain with a cylinder zone. Both the rotation domain and the tower are placed in the dynamic domain. In this study, a hybrid strategy for the numerical grid system has been implemented, unstructured grids have been employed in the dynamic domain, while structured grids have been utilized in the extraneous flow domain.

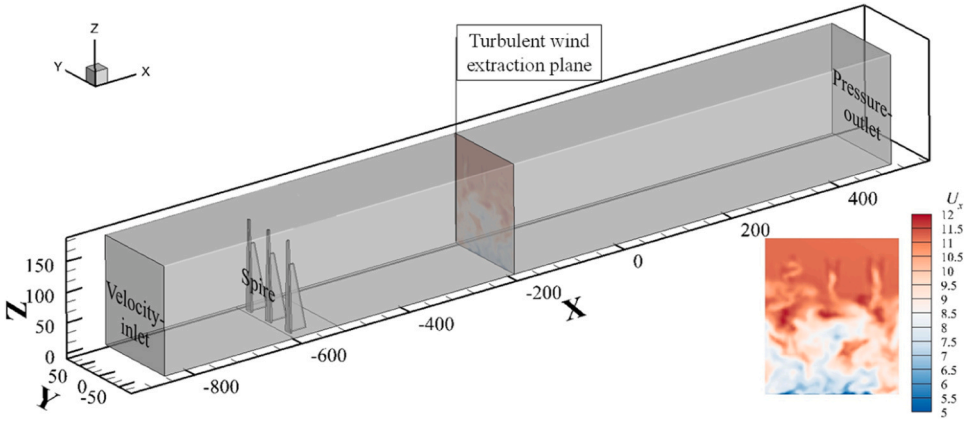


Fig. 3. Configuration of the computational domain for the generation of ABL flow (unit: cm).

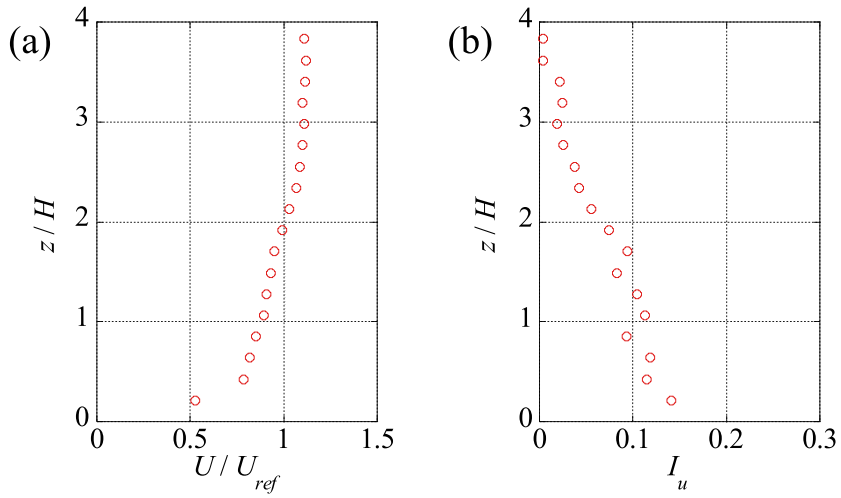


Fig. 4. Turbulent wind characteristics at the extraction plane: (a) mean wind speed; (b) turbulence intensity.

To handle the rotation region in the computational domain, the sliding grid has been widely utilized in Fluent [41] and it is very popular in the numerical simulation of rotating machines, such as wind turbine and turbomachinery. It allows the motion of rotation domain to simulate the rotating machines while keeps the non-rotation domain stationary. The flow field information exchange is achieved by interpolating the data at the centroids of the cells on either side of the sliding interface.

The dynamic mesh technique offers the ability to adjust mesh geometry to account for changes in the flow field during the calculation process. Three methods including the smoothing method, dynamic layering method, and local remeshing method, are available in the Fluent [41] to update the volume grid in the deforming regions. In this study, the diffusion smooth method is utilized to achieve a balance between numerical accuracy and cost efficiency.

The determination of grid node positions is achieved through the solution of the diffusion equation, which is expressed as follows:

$$\nabla\cdot(\gamma\nabla\vec{u}) = 0 \tag{6}$$

where $\vec{u}$ is the grid velocity, γ represents the diffusion coefficient.

The computation of grid node positions at the succeeding time step is updating according to the following formula:

$$\vec{x}_{new} = \vec{x}_{old} + \vec{u}\cdot t \tag{7}$$

In order to calculate the diffusion coefficient, the following method is employed.

$$\gamma = \frac{1}{V^{\alpha}} \tag{8}$$

where α is defined as the value between 0 and 2, V shows the normalized grid volume.

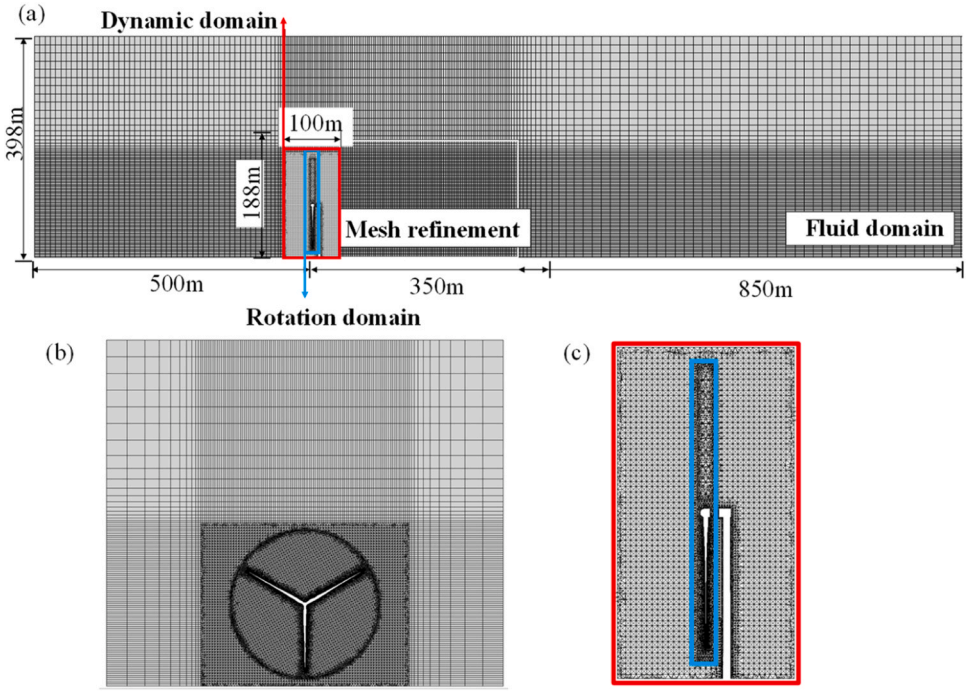


Fig. 5. Numerical grids for: (a) the whole fluid domain; (b) the slice at the place of wind turbine; (c) the rotation and the dynamic domains.

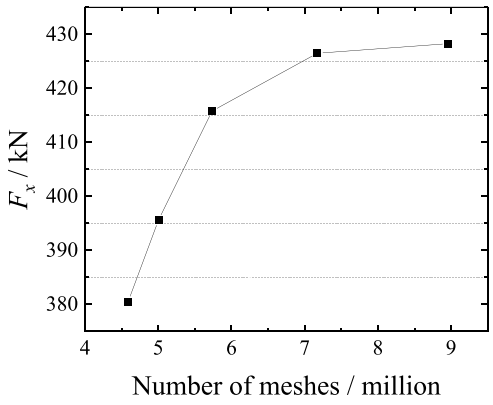


Fig. 6. Variations of the thrust force with the total number of numerical grids.

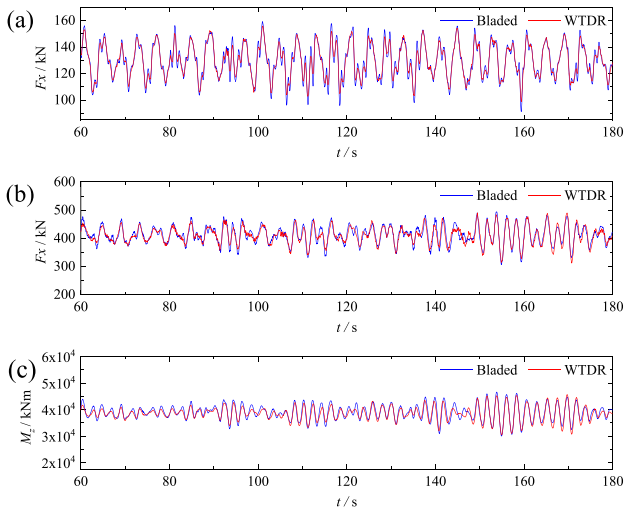


Fig. 7. Comparisons of aerodynamic forces calculated by CFD simulations and Bladed: (a) thrust force on the blade root; (b) thrust force on the tower base; (c) bending moment on the tower base.

2.4. Solution methods

The unsteady three-dimensional governing equations are evaluated using ANSYS Fluent 2022 software [41], employing the finite volume method (FVM). The convective and viscous terms in the momentum equations are discretized using the second-order central difference scheme, while the unsteady terms are discretized using the second-order implicit scheme. To decouple the solution of pressure and velocities, the semi-implicit pressure linked equations (SIMPLE) algorithm is utilized.

2.5. Grid independency analysis and verifications

The grid independence analysis is an indispensable step in CFD simulations, as it plays a crucial role in determining the optimal grid size and quality in various regions that impact the accuracy of the simulation results. The selection of an appropriate grid size and quality is essential to maintain a balance between the accuracy and the computational cost. In this study, the chordal and spanwise grid sizes of the blade are gradually increased, leading to the creation of four additional grid systems that comprise 4.589 million, 5.003 million, 5.736 million, and 8.962 million grids. During one complete rotation of the blade at 10 rpm and with an inflow wind velocity of 10 m/s, the axial thrust force on the tower base can be calculated. Fig. 5 depicts that, as the grid quality improves, the variation in thrust force tends to stabilize once the total number of grids exceeds 7 million. The relative error of the last two grid cases is 0.42%, which satisfies the criteria for grid independence. To optimize computational efficiency, the fourth grid system is selected for further investigation.

To validate the accuracy of the CFD simulations, a comparison is made between the aerodynamic loads obtained by CFD simulations and the commercial software GH Bladed [23]. The turbulent inflow condition is similar to the previous study carried out by Liu et al. [16] and the vertical profiles of mean wind speed and turbulence intensity are validated by experiments as well. Subsequently, the mean wind speed and the turbulence intensity at the hub height are used as the wind condition entering the commercial software GH Bladed. The comparison is focused on the thrust forces on the blade root and tower base, as well as the bending moment on the tower base. Fig. 6 illustrates that the results obtained from both approaches exhibit a high degree of similarity, thus indicating the credibility and accuracy of the CFD simulations performed in this study. .

3. Fluid-structure interaction

3.1. Computational structural dynamics

Liu et al. [16] proposed a structural dynamic model for wind turbines with 8 degrees of freedom utilizing a generalized coordinate system, as shown in Fig. 8. The tower and nacelle are represented by a global

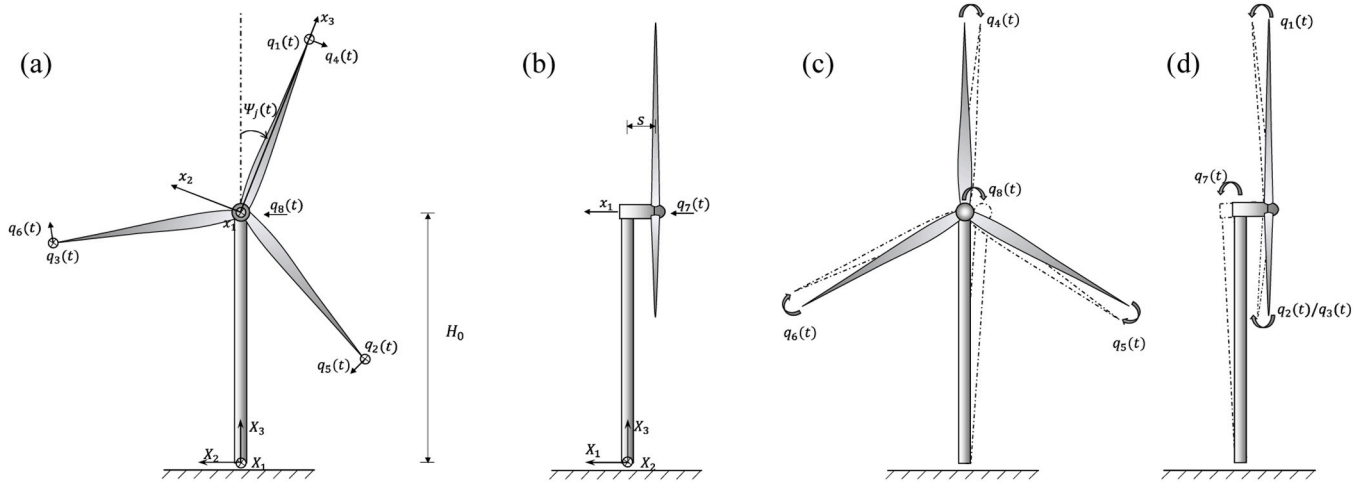


Fig. 8. The DoFs for the CSD model: (a,c) in the front view and; (b,d) in the side view.

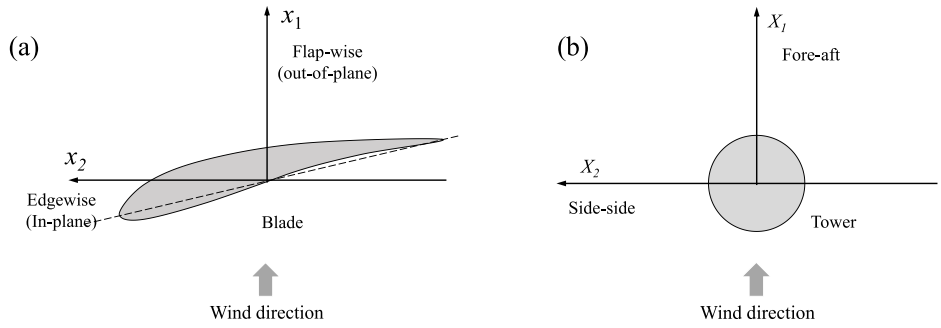


Fig. 9. The coordinate systems on the: (a) blade and; (b) tower.

coordinate system (X_1, X_2, X_3) with its origin located at the tower base and the X_1, X_2, and X_3 directions corresponding to the windward, sideward, and upward directions, respectively. For each blade, a local coordinate system (x_1, x_2, x_3) is employed with its origin located at the root of the blade and x_1, x_2, and x_3 directions representing flap-wise, edgewise, and spanwise directions, respectively, in Fig. 9. Deflections of three blades along the x_1 and x_2 axes are denoted by $q_1(t) \sim q_3(t)$ and $q_4(t) \sim q_6(t)$ while the deflection of the tower along X_1 and X_2 axes is represented by $q_7(t)$ and $q_8(t)$. The azimuth angle of the local coordinate system for each blade is determined by the rotational speed and can be expressed as follows:

$$\Psi_j(t) = \Omega t + \frac{2\pi}{3}(j-1) j = 1,2,3 \tag{9}$$

where Ω is the blade rotational velocity.

The wind turbine system is composed of 8 DoFs, amongst which 6 are ascribed to the blades, whereas the remaining 2 are assigned to the tower. These DoFs are expressed as follows:

$$\mathbf{q}(\mathbf{t}) = \left[\mathbf{q}_l(t) \;\; \mathbf{q}_g(t)\right]^{\mathrm{T}} \tag{10}$$

$$\mathbf{q}_l(t) = [q_1(t) \ldots q_6(t)]^{\mathrm{T}}$$

$$\mathbf{q}_g(t) = [q_7(t) \;\; q_8(t)]^{\mathrm{T}} \tag{11}$$

The displacements of the jth blade at the blade root, including flap-wise motions and the edgewise motions can be represented as follows:

$$\left.\begin{array}{l} \overline{d}_{1,j}(x_3,t) = \Phi_{1B}(x_3) q_j(t) \\ \overline{d}_{2,j}(x_3,t) = -\Phi_{2B}(x_3) q_{j+3}(t) \end{array} \quad j = 1,2,3 \right\} \tag{12}$$

where $\Phi_{1B}(x_3)$ and $\Phi_{2B}(x_3)$ show the first mode shape in the flap-wise and edgewise directions.

The corresponding velocity components can be expressed as follows:

$$\left.\begin{array}{l} \dot{d}_{1,j}(x_3,t) = \dfrac{d}{dt}\overline{d}_{1,j}(x_3,t) = \Phi_{1B}(x_3)\dot{q}_j(t) \\ \dot{d}_{2,j}(x_3,t) = \dfrac{d}{dt}\overline{d}_{2,j}(x_3,t) = -\Phi_{2B}(x_3)\dot{q}_{j+3}(t) \end{array} \quad j = 1,2,3 \right\} \tag{13}$$

It is noteworthy that the rotational motion of the blade can have an impact on the velocity component in the x_2 direction, and thus, it is necessary to consider this effect in the analysis.

$$\overline{d}_{2,j}(x_3,t) = -x_3\Omega \tag{14}$$

In the global coordinate system, the velocity field around blades is influenced by movements of the tower and nacelle. This impact can be mathematically expressed as follows:

$$\dot{d}_{1,j}\left(x_3,t\right) = \dot{q}_7(t)$$

$$\dot{d}_{2,j}\left(x_3,t\right) = \cos\Psi_j \dot{q}_8(t)$$

$$\dot{d}_{3,j}\left(x_3,t\right) = -\sin\Psi_j \dot{q}_8(t) \tag{15}$$

In addition, it is essential to account for the contribution of the angular rotation $\theta(t)$ at the tower top. Its effect to the velocity vector in the local coordinate system is represented as follows:

$$\dot{d}_{1,j}(x_3,t) = x_3\cos\Psi_j\dot{\theta}(t)$$

$$\dot{d}_{2,j}(x_3,t) = \sin\Psi_j s\dot{\theta}(t)$$

$$\dot{d}_{3,j}(x_3,t) = \cos\Psi_j s\dot{\theta}(t) \tag{16}$$

The velocity components of the jth blade in the local coordinate system can be expressed as follows:

$$\left.\begin{array}{c} \dot{d}_{1,j}\left(x_3,t\right) = \Phi_{1B}(x_3)\dot{q}_j(t) + \dot{q}_7(t) + x_3\cos\Psi_j\dot{\theta}(t) \\ \dot{d}_{2,j}\left(x_3,t\right) = -\Phi_{2B}(x_3)\dot{q}_{j+3}(t) - x_3\Omega + \cos\Psi_j\dot{q}_8(t) + \sin\Psi_j s\dot{\theta}(t) \\ \dot{d}_{3,j}\left(x_3,t\right) = -\sin\Psi_j\dot{q}_8(t) + \cos\Psi_j s\dot{\theta}(t) \end{array} \right\} \tag{17}$$

Then, the total kinetic energy is calculated.

$$\begin{aligned} \mathrm{T}(\mathbf{q}(t),\dot{\mathbf{q}}(t)) = {} & \frac{1}{2}\sum_{j=1}^{3}\int_0^{L_B}\mu_j(x_3)\left(\dot{d}_{1,j}^2(x_3,t) + \dot{d}_{3,j}^2(x_3,t) + \dot{d}_{3,j}(x_3,t)\right)dx_3 \\ & + \frac{1}{2}\int_0^{H_0}\mu_{\mathrm{T}}(X_3)\dot{d}_{X_1}^2\left((X_3,t) + \dot{d}_{X_2}^2(X_3,t)\right)dX_3 \\ & + \frac{1}{2}M_0\left(\dot{q}_7^2(t) + \dot{q}_8^2(t)\right) \end{aligned} \tag{18}$$

where $\mu_{\mathrm{T}}(X_3)$ shows the mass per unit length of the tower, M_0displays the mass of nacelle.

The potential energy is expressed as follows:

$$U(\mathbf{q}(t)) = \frac{1}{2}\mathbf{q}^{\mathrm{T}}(t)\mathbf{K}_s\mathbf{q}(t) \tag{19}$$

where $\mathbf{K}_s$is the structural stiffness matrix, including the centrifugal hardening of rotating blades.

The expression for the Euler-Lagrange stationary condition is shown.

$$\frac{\partial}{\partial t}\left(\frac{\partial \mathrm{T}}{\partial \dot{\mathbf{q}}}\right) - \frac{\partial \mathrm{T}}{\partial \mathbf{q}} + \frac{\partial \mathrm{U}}{\partial \mathbf{q}} = \frac{\partial \mathrm{W}}{\partial \mathbf{q}} - C\dot{\mathbf{q}} \tag{20}$$

The equation of motion for the wind turbine can be derived according to Euler-Lagrange stationary condition.

$$\mathbf{M}(t)\ddot{\mathbf{q}}(t) + \mathbf{C}\dot{\mathbf{q}}(t) + \mathbf{K}\mathbf{q}(t) = \boldsymbol{Q}(\dot{\mathbf{q}}(t),t) \tag{21}$$

where M(t), C, and K show the mass, damping and stiffness matrices

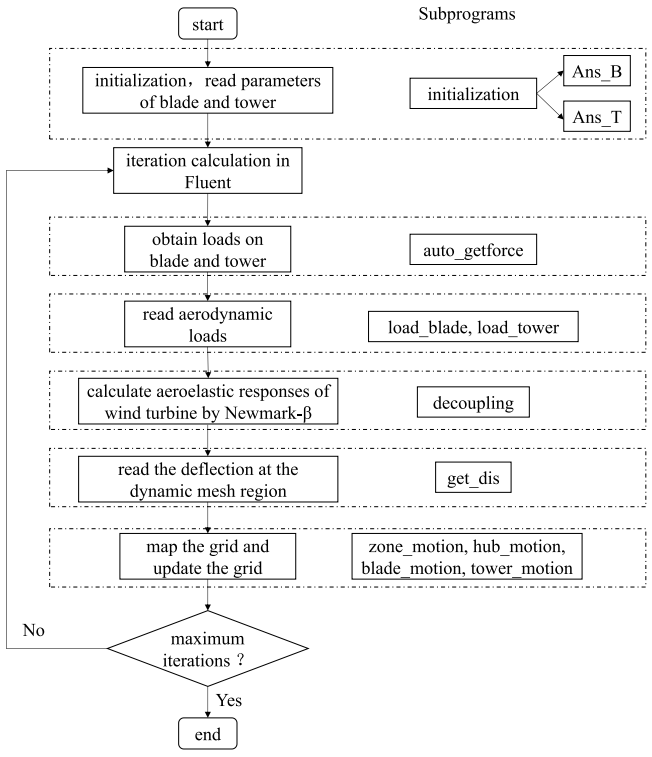


Fig. 10. A framework of the two-way FSI for wind turbine.

which will be introduced in the previous study [16], Q(q(t),t) is the external force.

Finally, the equations of motion can be solved by the Newmark-β approach.

3.2. Fluid-structure interaction

A FSI analysis framework for wind turbines has been proposed by integrating CFD simulations and the structural dynamic model, as illustrated in Fig. 10. Once parameters, including those related to the blade and tower, are initialized, the CFD simulation in Fluent commences. The aerodynamic loads for both the blades and the tower are calculated, which are then implemented in the structural dynamic model to compute displacements of all components, utilizing the Newmark-β method. These calculated displacements are then incorporated back into the CFD simulation, where the numerical grids are modified and updated. The process iterates until maximum iterations have been achieved.

3.3. Verification of the FSI model

As show in Fig. 11, the flap-wise and edgewise displacements at the blade tips, as well as the fore-aft and side-side displacements at the tower top are calculated by the proposed FSI model and the commercial software Bladed [23]. It should be noted that the displacements calculated by both methods are one-way FSI which means that all components of wind turbine are rigid during the CFD simulation. The results obtained from both methods are consistent with each other, proving the accuracy of the proposed FSI model in predicting wind turbine displacement.

4. Results and discussion

4.1. Case settings

This study investigates the aerodynamic loads and aeroelastic responses of a wind turbine in both uniform and turbulent winds through a FSI model. The 4.5 MW wind turbine used in this study is a real wind turbine, and the structural properties of blade and tower are provided by the manufacturer. Additionally, the influence of different blade and tower flexibility is also explored. A total of 16 cases are considered, with the first eight cases subjected to uniform winds and the latter eight exposed to turbulent winds. The DoFs of the blades and tower in the different directions are either considered or neglected in different cases, as summarized in Table 4. Case names are listed in the final column, with the “W” indicating the inflow condition, “T” representing the DoFs of tower, and “B” and “b” indicating the DoFs of blades in the flap-wise and edgewise directions, respectively. The numbers “1” and “0” encode whether the specific degree of freedom is either included or removed, respectively. For instance, W0T0B0b0 indicates the uniform inflow condition with all DoFs are removed, thus adopting the one-way fluid-structure interaction.

4.2. Aerodynamic loads on wind turbine

4.2.1. Time series of aerodynamic loads

The simulation time for cases examined in this study are set at 200 s and 250 s for uniform and turbulent wind conditions, respectively. Regarding cases conducted under turbulent winds, the wind turbine does not undergo rotation during the initial 50 s, thereby conserving computational resources. The last 80 s of the time series data are collected and utilized for subsequent statistical analysis.

Fig. 12 and Fig. 13 present the time series data for thrust forces acting on both blade root and tower base under uniform wind conditions. To facilitate comparison, the 25 s time series data for one blade is depicted. The cases of W0T0B0b0 (fully rigid) and W0T1B1b1 (fully flexible) function as reference groups and are included within every subfigure, as denoted in Fig. 12 and Fig. 13. The periodicity of the thrust

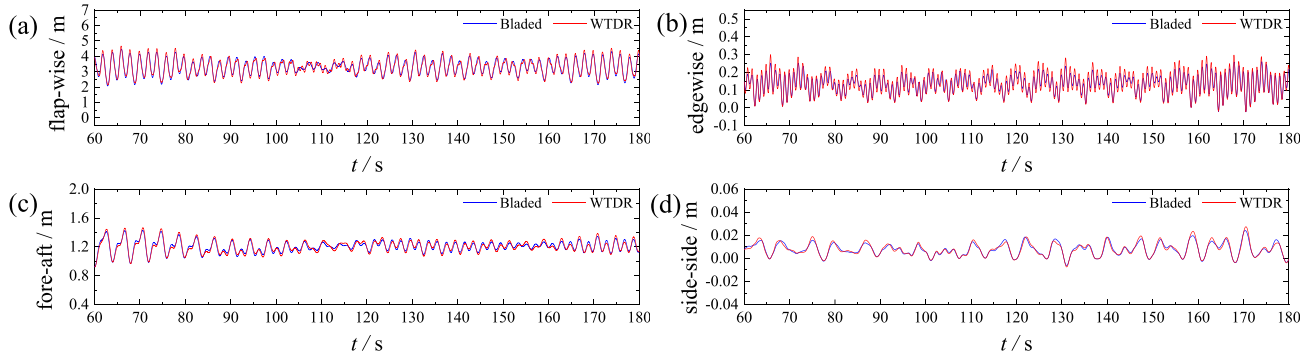


Fig. 11. Comparisons of displacements of wind turbines calculated by the FSI model and Bladed: (a) the flap-wise displacement at the blade tip; (b) the edgewise displacement at the blade tip; (c) the fore-aft displacement at tower top; (d) the side-side displacement at tower top.

Table 4
Case settings.

Case	Uniform inflow	Turbulent inflow	Tower motion	Flap-wise motions of blades	Edgewise motions of blades	Index
1	●	○	○	○	○	W0T0B0b0
2	●	○	○	○	●	W0T0B0b1
3	●	○	○	●	○	W0T0B1b0
4	●	○	○	●	●	W0T0B1b1
5	●	○	●	○	○	W0T1B0b0
6	●	○	●	○	●	W0T1B0b1
7	●	○	●	●	○	W0T1B1b0
8	●	○	●	●	●	W0T1B1b1
9	○	●	○	○	○	W1T0B0b0
10	○	●	○	○	●	W1T0B0b1
11	○	●	○	●	○	W1T0B1b0
12	○	●	○	●	●	W1T0B1b1
13	○	●	●	○	○	W1T1B0b0
14	○	●	●	○	●	W1T1B0b1
15	○	●	●	●	○	W1T1B1b0
16	○	●	●	●	●	W1T1B1b1

●: adopt this inflow condition or consider the corresponding DoFs
○: do not adopt this inflow condition or neglect the corresponding DoFs

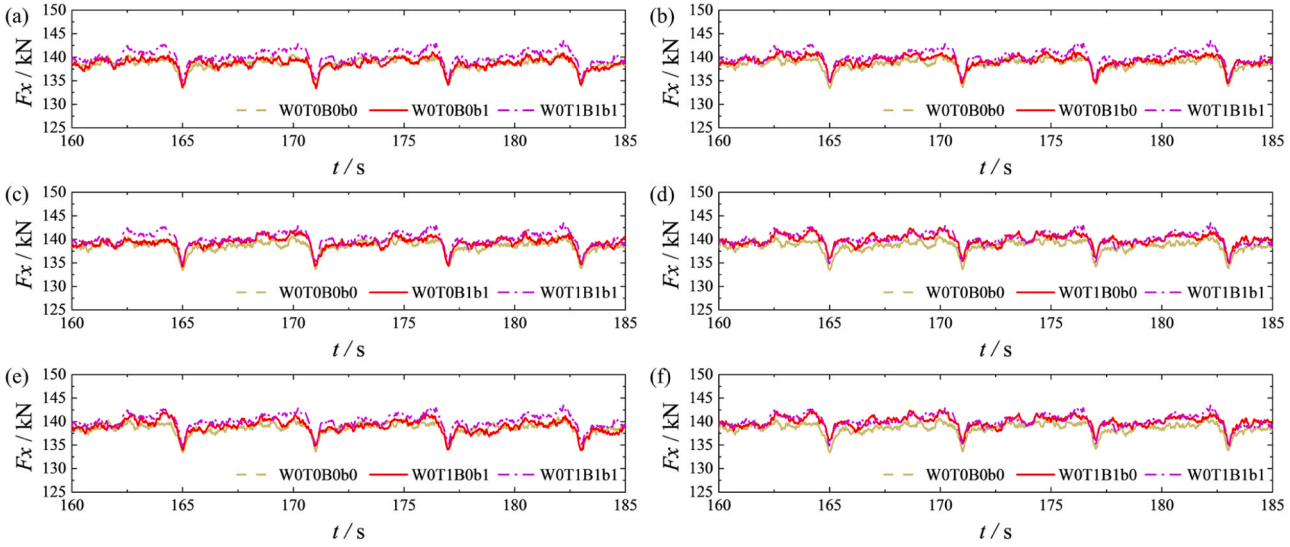


Fig. 12. Time series of the thrust force on the blade root considering different blade and tower flexibilities under uniform inflow condition.

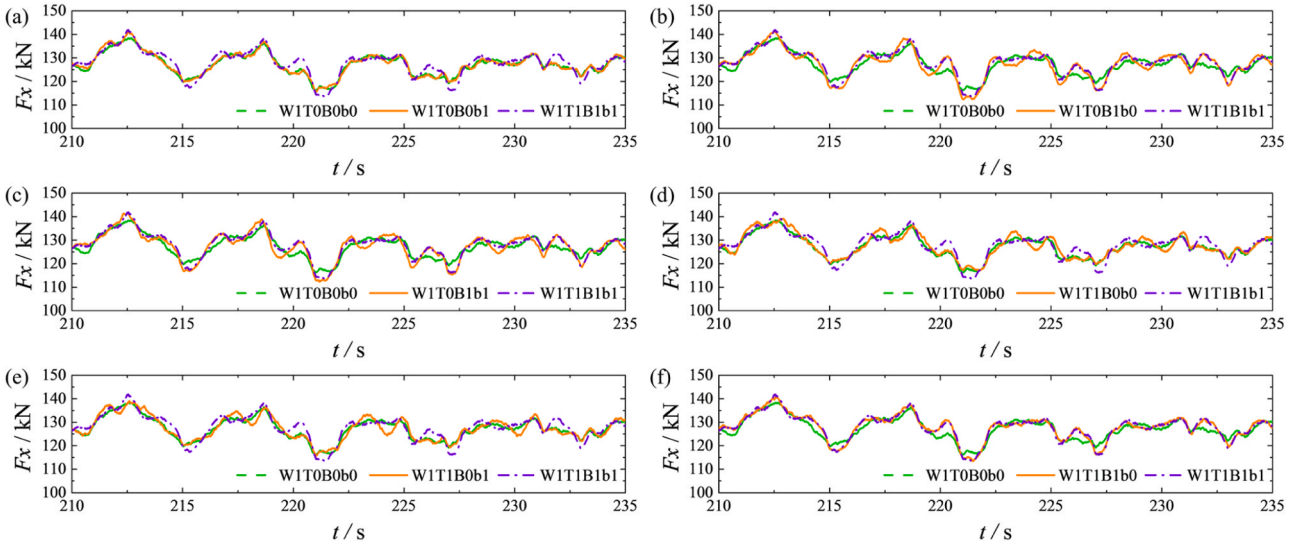


Fig. 13. Time series of the thrust force on the blade root considering different blade and tower flexibilities under turbulent inflow condition.

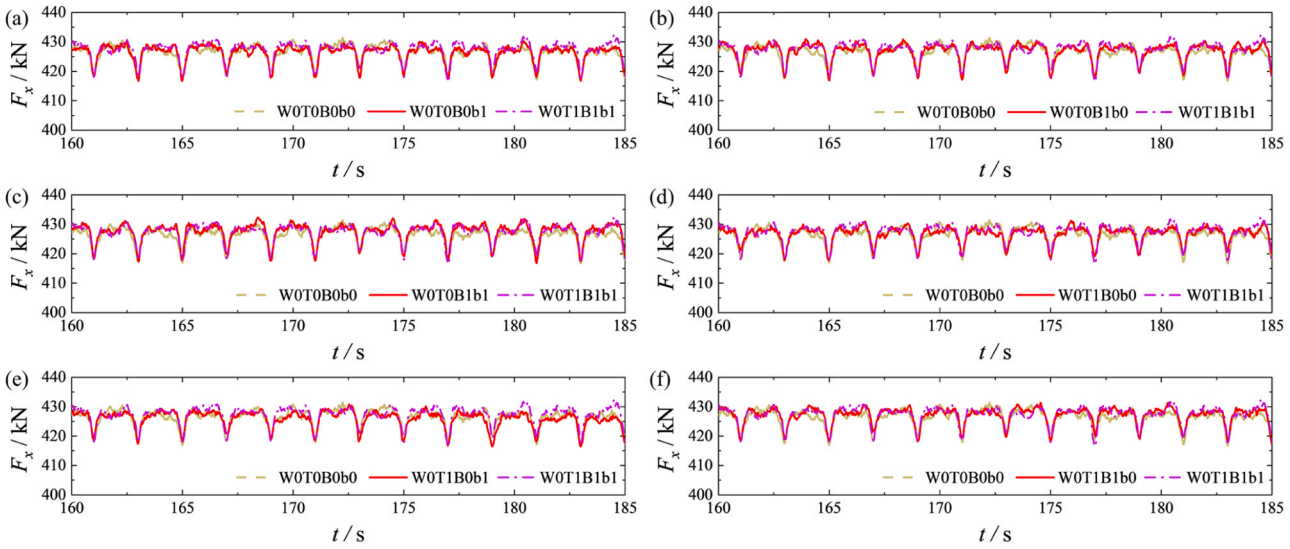


Fig. 14. Time series of the thrust force on the tower base considering different blade and tower flexibilities under uniform inflow condition.

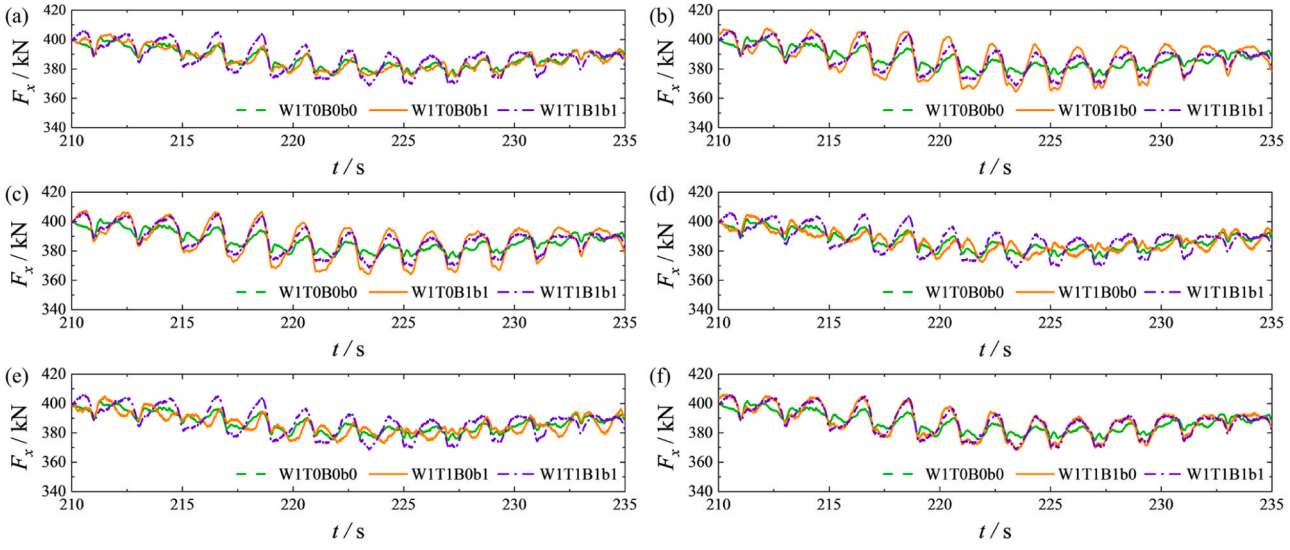


Fig. 15. Time series of the thrust force on the tower base considering different blade and tower flexibilities under turbulent inflow condition.

forces on both blade root and tower base is evident in uniform winds. The period of the thrust force on the blade root is clearly 1/3 of that on the tower base, resulting from rotations of the three blades. The blade rotational velocity is 10 RPM, signifying one rotation every 6 s and establishing a load cycle of approximately 6 s for a single blade and 2 s for the tower. The oscillations of the thrust force arise mainly from the three-dimensional rotating wind turbine blades.

Regarding the thrust force on the blade root under uniform winds, it is apparent that the fully flexible case (W0T1B1b1) yields higher values compared to the fully rigid case (W0T0B0b0). As demonstrated in Fig. 12(d) and Fig. 12(f), the time series data on the blade root under cases of W0T1B1b0 and W0T1B0b0 respectively, have similar amplitudes as that of the fully flexible case (W0T1B1b1), which illustrates the significant impact of tower motion upon the thrust force. Conversely, the time series data for thrust force on the blade root under case W0T0B0b1 matches well with the fully rigid working condition (W0T0B0b0) results, as blade motions in the edgewise direction have little impact on the thrust force. The primary factor contributing to the differing patterns within each figure is the disparate states of the blades and tower. When the blades are flexible in the flap-wise direction, they demonstrate a state of backward bending, while a flexible tower causes an elevation angle of the rotor disk. Pertaining to the thrust force on the tower base, only slight differences are observed between different cases which suggests that thrust force on the tower base under uniform inflow condition does not display strong sensitivity to the motion of the tower and blades, as depicted in Fig. 13.

Under turbulent winds in Fig. 14, the thrust forces on the blade root demonstrate similarity across different cases, indicating their insensitivity to the motions of the blade and tower. In Fig. 15(b) and Fig. 15(c), compared with the rigid case denoted as W1T0B0b0, the time series of thrust force on the tower base under cases W1T0B1b0 and W1T0B1b1 exhibit larger amplitudes which implies that the motions of blades in the flap-wise direction have an essential effect. The case W1T0B0b1 in Fig. 15(a) is basically consistent with the fully rigid case while the time series of thrust forces in case W1T1B1b0 in Fig. 15(f) is similar to the fully flexible case. This considerable difference arises from the disparity in the flap-wise and edgewise stiffness of the blade, resulting in the greater flap-wise displacement and higher disturbance of the surrounding flow field during vibration. With the addition of DoFs of the tower, the impact of load fluctuation is partially reduced. This

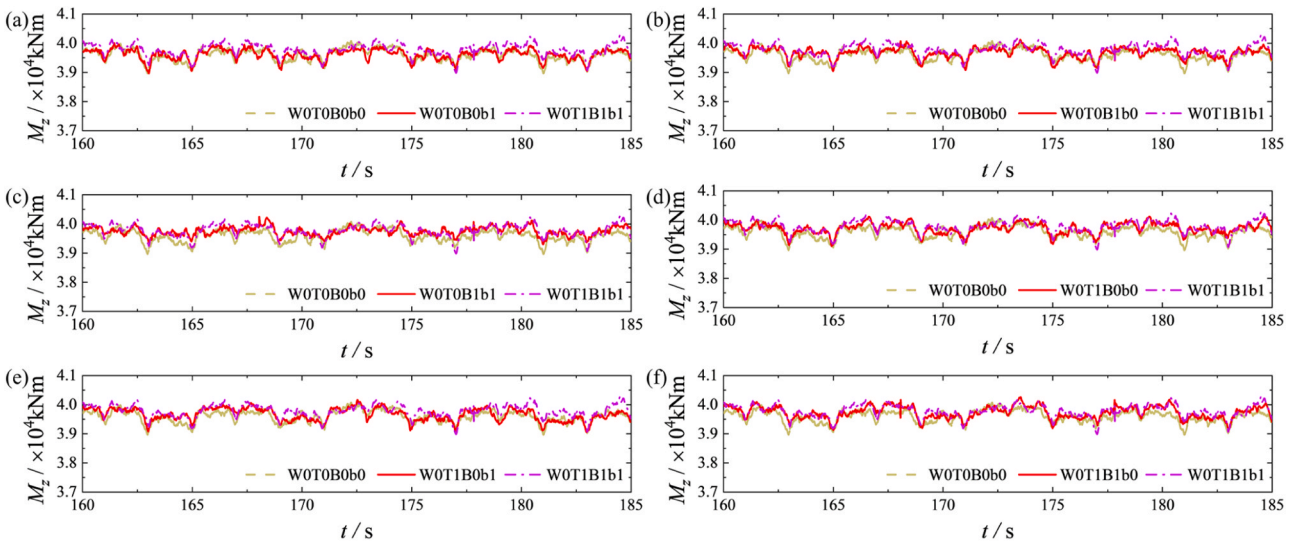


Fig. 16. Time series of the bending moment on the tower base considering different blade and tower flexibilities under uniform inflow condition.

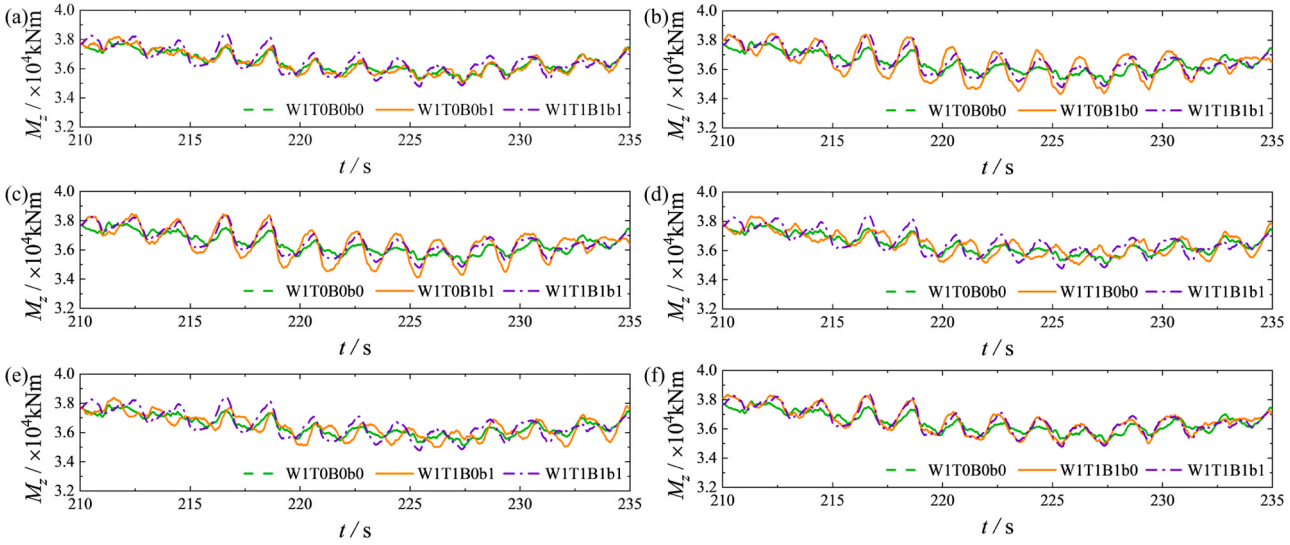


Fig. 17. Time series of the bending moment on the tower base considering different blade and tower flexibilities under turbulent inflow condition.

phenomenon can be attributed to the difference in vibration frequency between the tower and blade, which operates akin to a damper installed on the blades to reduce absolute vibration amplitude and the thrust force. The tower base is firmly installed on the ground while the blade tip enjoys a degree of unrestricted mobility. Consequently, the pliant nature of the tower can be analogously likened to a damper, positioned between the ground and the blade, effectively ameliorating the vibrational dynamics of the blade. On the contrary, the flexible blade cannot be considered as a damper, as its tip retains the capacity for unimpeded oscillation, rendering it incapable of imparting any damping effect. This phenomenon is more pronounced on the thrust force on the tower base since it is the accumulation of aerodynamic loads on blades.

Fig. 16 and Fig. 17 display the time series of bending moments at the tower base in both uniform and turbulent wind conditions. In contrast to the thrust force, the periodic behavior of the bending moment under uniform inflow conditions exhibits less conspicuous regularity. The thrust forces acting upon the three blades do not exhibit synchronous variations; while the thrust force at any given blade root reaches its minimum when aligned with the position directly in front of the tower, the thrust forces at the remaining two blade roots remain relatively constant. Furthermore, the force arms associated with the thrust forces on the three blade roots exhibit minor variations. The bending moments experienced at the tower base are collectively induced by the concurrent action of thrust forces on all three blade roots. This phenomenon constitutes the primary contributing factor to the comparatively reduced periodicity observed in the bending moment under uniform inflow conditions. The variations in bending moments across different scenarios are inconsequential, indicating their minimal susceptibility to blade and tower flexibility. Concerning the bending moments under turbulent inflow scenarios, they bear a resemblance to the thrust force. Notably, they are significantly affected by the flap-wise motions of blades, with the influence of the edgewise motions of blades being negligible. The decrease in bending moment amplitude when the motions of both the blade and tower are taken into account aligns with the aforementioned findings which implies the necessity of FSI analysis and the proper choice of the DoFs for wind turbine.

4.2.2. *Statistical features of aerodynamic loads*

As time series curves are unable to provide a quantitative depiction of the statistical characteristics of aerodynamic loads, however, the box plots can and are displayed in Fig. 18. The plot consists of a rectangular box that represents the middle 50% of the data. The bottom of the box is

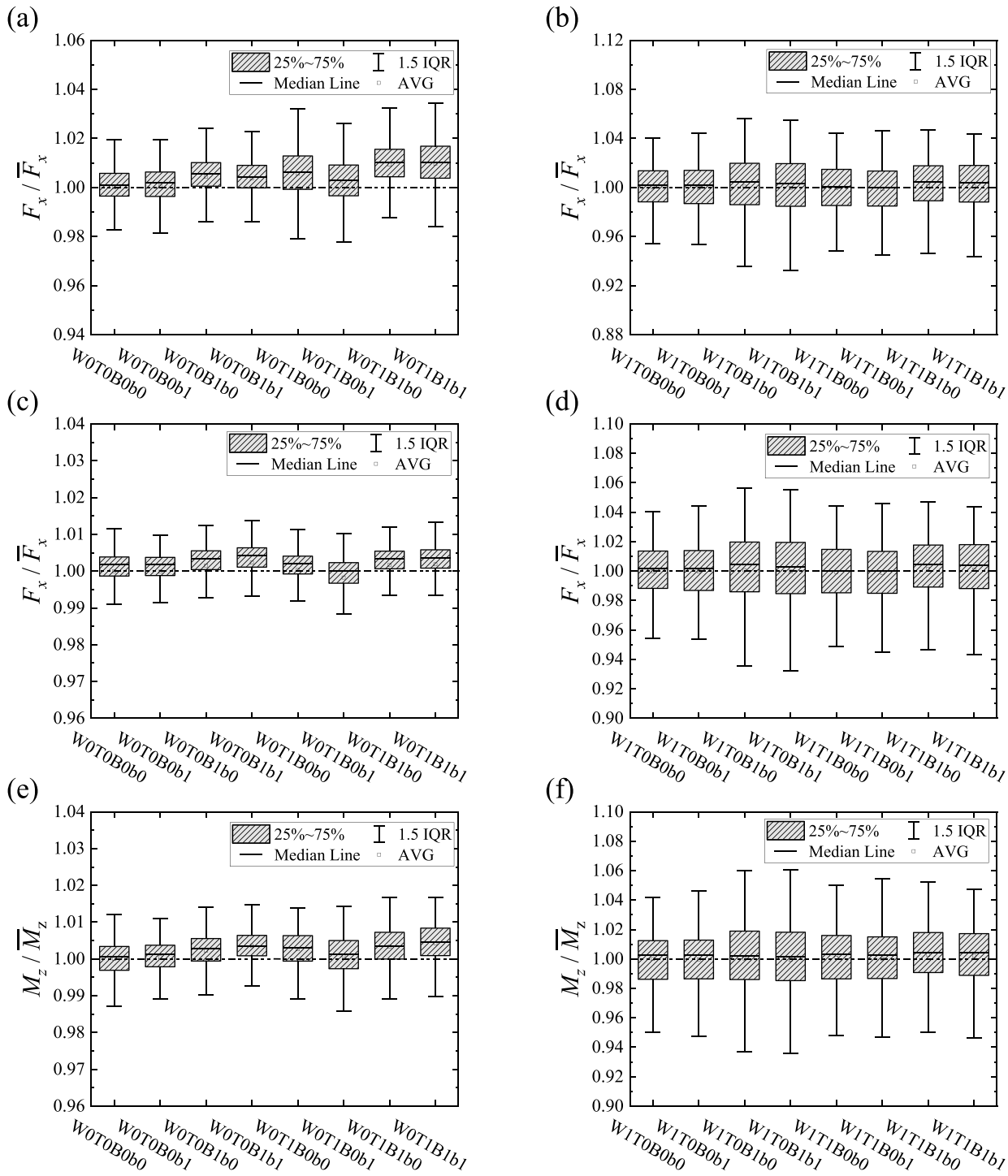


Fig. 18. Box plots of: (a) the normalized thrust force at the blade root under uniform and; (b) turbulent winds; (c) the normalized thrust force at the tower base under uniform and; (d) turbulent winds; (e) the normalized bending moment at the tower base under uniform and; (f) turbulent winds.

the 25th percentile, also known as the first quartile (Q1), and the top of the box is the 75th percentile, or the third quartile (Q3). A horizontal line (the median) is drawn in the box to show the position of the middle value. The "whiskers" extend from the top and bottom of the box to represent the range of the data. Normally, they represent 1.5 times the interquartile range (IQR). Employment of this tool assists in the observation of the presence of data gaps, and assessment of the asymmetry of distribution. Box plots can also serve as a comprehensive tool in the comparison of multiple data sets, by illustrating the differences and similarities inherent among these data sets through the inclusion of multiple box plots on a singular chart.

For comparison purposes, the aerodynamic loads have been normalized by the averaged wind loads under the fully rigid case. The results presented in Fig. 18(a) indicate that the average and median values of thrust force on the blade root show an increase due to blade and tower motions under uniform inflow condition. The IQR, maximum and minimum values will not change extensively if only the motions of blade are considered in the FSI model, but the addition of tower motion increases these values. It is interesting to note that the median, average and the maximum values are lower than other three cases when both

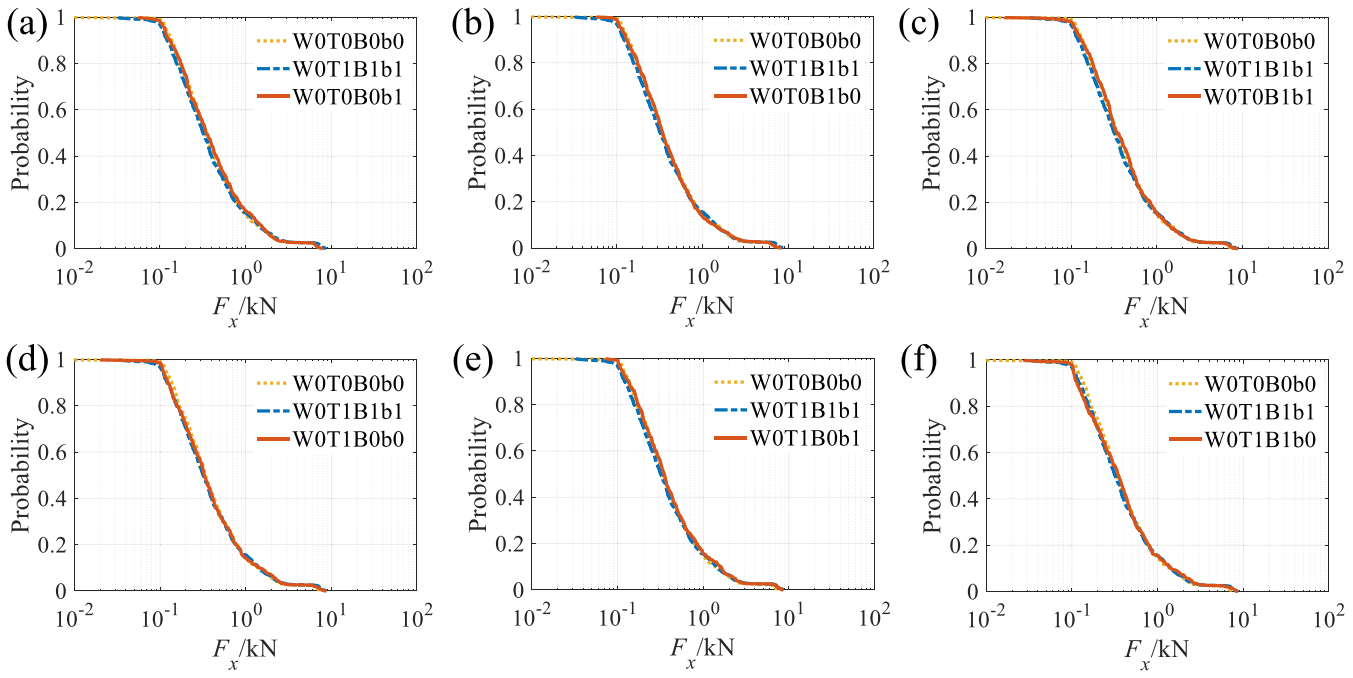


Fig. 19. Exceedance probabilities of the thrust force at the blade root considering different blade and tower flexibilities under uniform inflow condition.

tower motion and the edgewise motion of blade are considered which may be induced by the coupling effect. Similarly, under turbulent inflow condition, blade motions clearly raise the median, the IQR, maximum and minimum values of thrust force on the blade in Fig. 18(b) which implies that the large fluctuation of thrust force. When the tower motions are added, the maximum and minimum values for the last four cases decrease and maintain the similar values. It is noted that the cases considering the tower motion and the flap-wise motion of blade have similar statistical features with the fully flexible cases under the same inflow condition. Comparing with the uniform inflow condition, the IQR, maximum and minimum values increase which shows that the fluctuation amplitude of the thrust force increases. The median and average decreases since the averaged wind speed acting on the rotor disk is smaller under ABL turbulent winds. For the thrust force and bending moment on the tower base as shown in Fig. 18 (c) (d) and Fig. 18 (e) (f), the similar trend can be observed.

In summary, the aerodynamic loads are significantly influenced by blade and tower flexibility when subjected to uniform inflow condition, with particular sensitivity observed in blade flap-wise motions. The effects of turbulence on aerodynamic loads result in increased fluctuations, with the flap-wise motions of blades found to be more critical to load magnitude compared to edgewise motions. The inclusion of tower

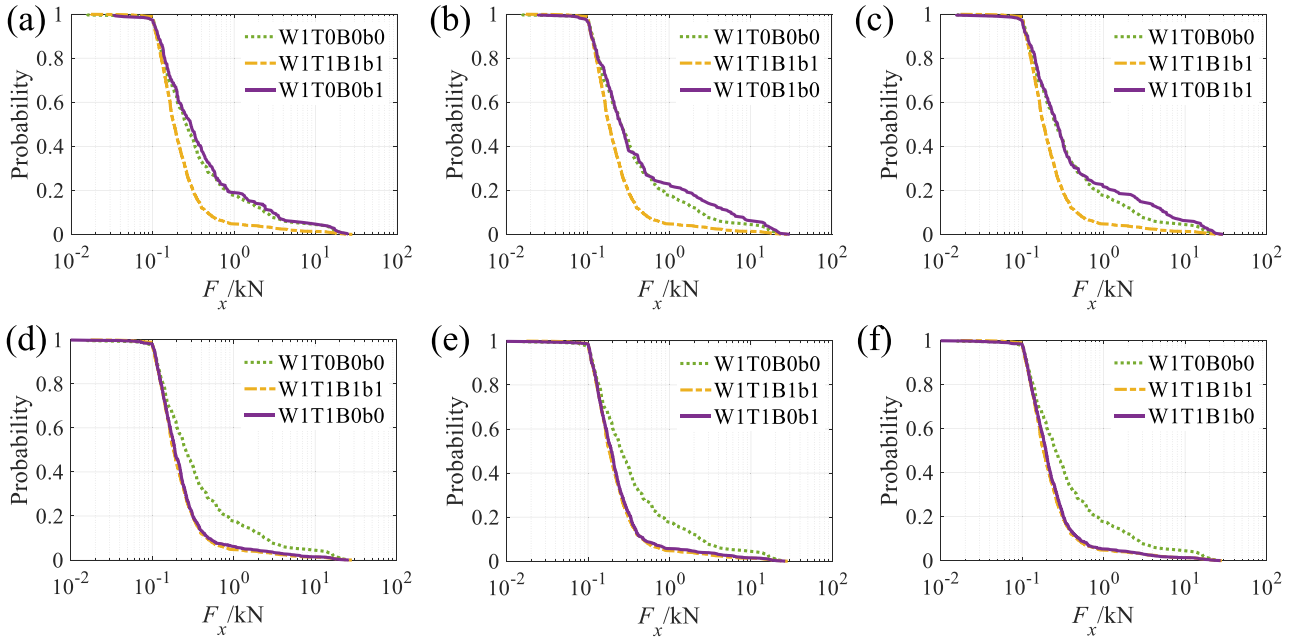


Fig. 20. Exceedance probabilities of the thrust force at the blade root considering different blade and tower flexibilities under turbulent inflow condition.

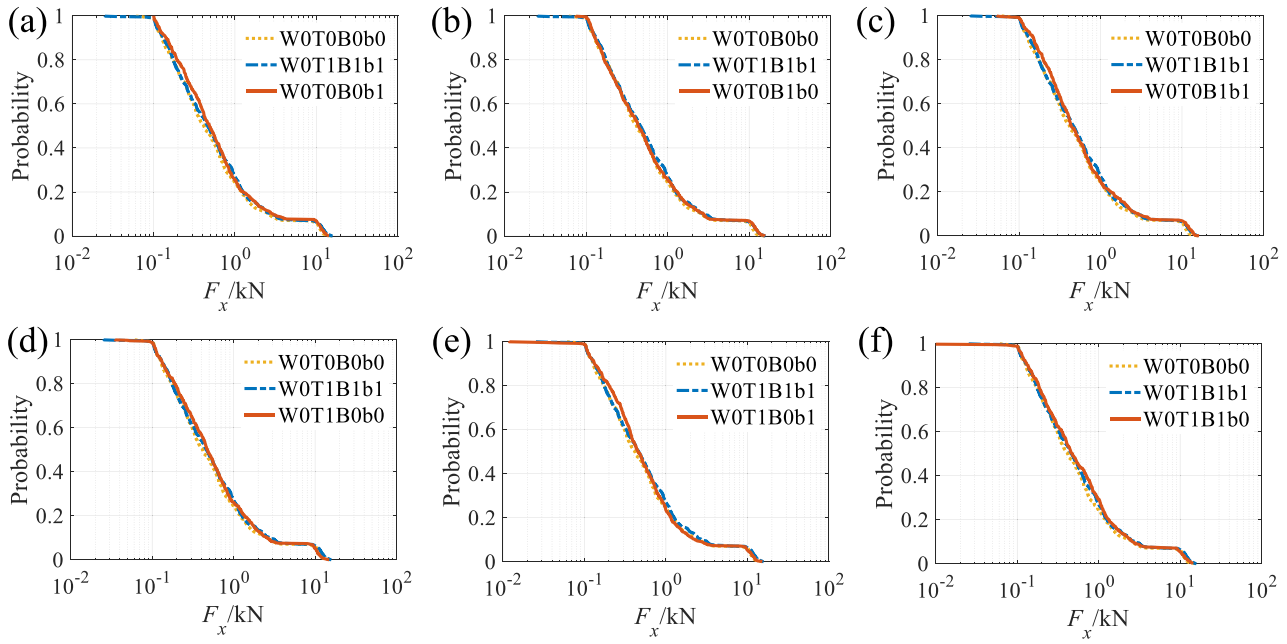


Fig. 21. Exceedance probabilities of the thrust force at the tower base considering different blade and tower flexibilities under uniform inflow condition.

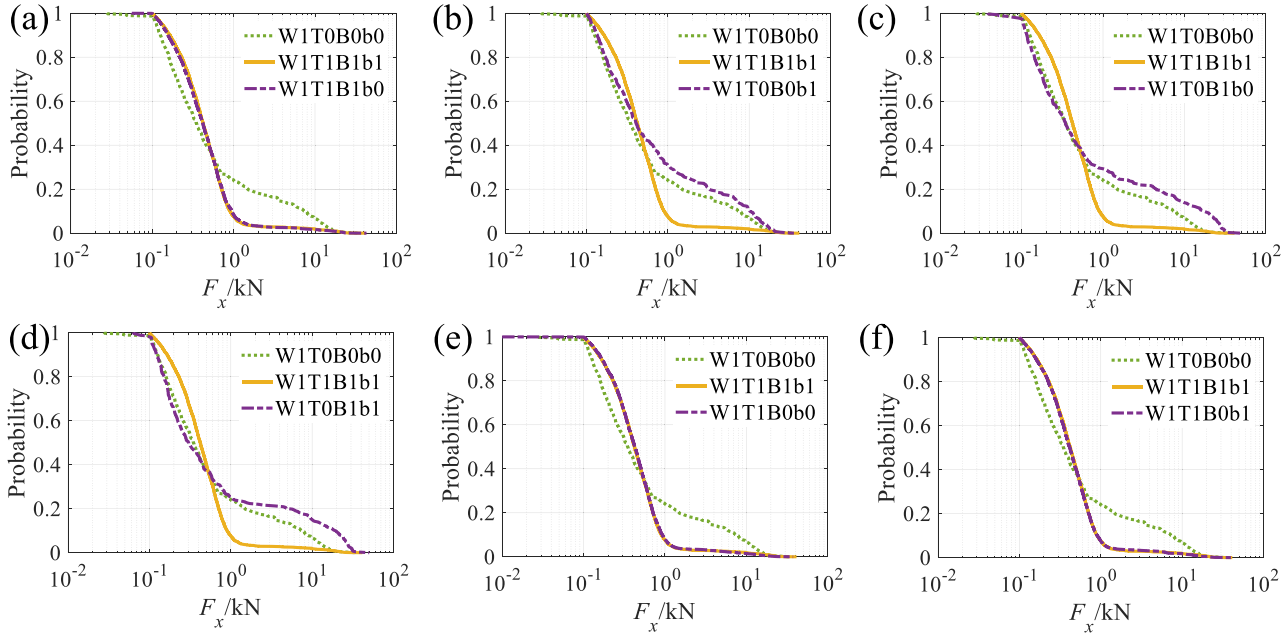


Fig. 22. Exceedance probabilities of the thrust force at the tower base considering different blade and tower flexibilities under turbulent inflow condition.

motion mitigates this sensitivity to some extent through coupling effects. Therefore, it is crucial to undertake a comprehensive fluid structure interaction analysis of wind turbines.

4.2.3. Exceedance probability of aerodynamic loads

In addition, the rainflow counting method is employed to investigate the exceedance probability of aerodynamic loads. The amplitude and cycle times are counted and subsequently used to calculate the exceedance probability. The results are presented in Fig. 19 to Fig. 24, which illustrate the exceeding probability of both the thrust force on the blade root and tower base as well as the bending moment on the tower base under uniform and turbulent inflow conditions.

Under uniform inflow conditions, the exceedance probability curves of the aerodynamic loads demonstrate consistent trends, highlighting similar fatigue loads experienced by the wind turbines. Under turbulent conditions, the loads vary considerably, particularly when the flap-wise motions of blades are taken into account without accounting for the movements of tower. Significantly, the amplitude of the load occupies a broader distribution range, with the maximum amplitude being notably higher than other cases. Fig. 20(b)(c) illustrate this result, depicting the maximum thrust force amplitude of approximately 30 kN, which is approximately 7.1% higher than that of the fully flexible case (W1T1B1b1). Similar trends are displayed in Fig. 22(b)(c), showing the maximum thrust force amplitude increase of roughly 22.0% at the tower

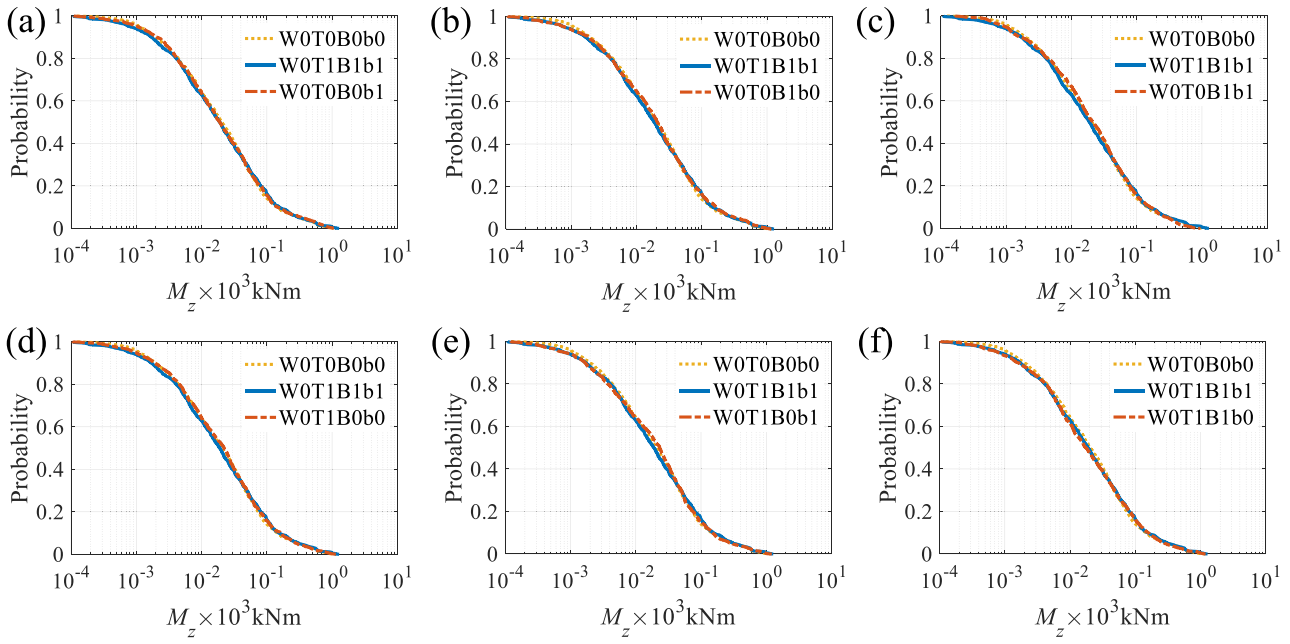


Fig. 23. Exceedance probabilities of the bending moment at the tower base considering different blade and tower flexibilities under uniform inflow condition.

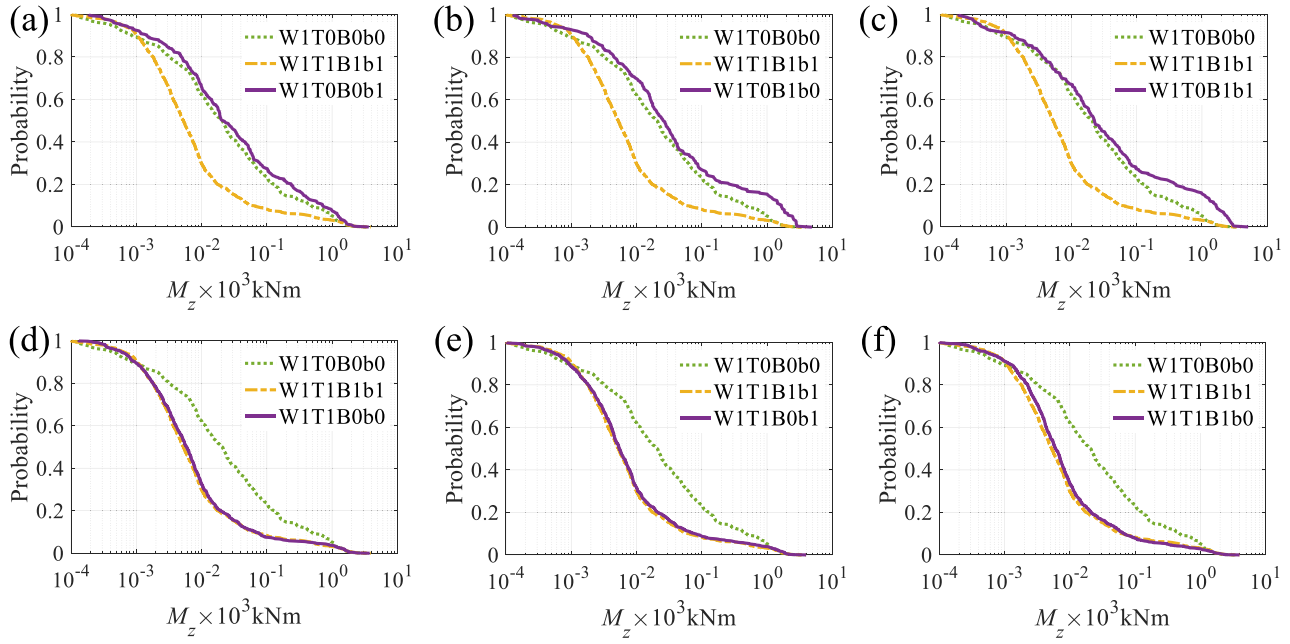


Fig. 24. Exceedance probabilities of the bending moment at the tower base considering different blade and tower flexibilities under turbulent inflow condition.

base when compared to the fully flexible case. Furthermore, Fig. 24(b)(c) portray the maximum bending moment amplitude maintain 4.9×10^3 kNm and 5.1×10^3 kNm, respectively, which equates to an increase of about 18.4% and 22.4% regarding the fully flexible case. The exceedance probability curves overlap with that for the fully flexible case when the DoFs of tower are added in Fig. 20(d)(e)(f), Fig. 22(d)(e)(f), and Fig. 24(d)(e)(f).

4.2.4. *Equivalent fatigue loads*

The equivalent fatigue loads under different inflow conditions considering variations in blade and tower flexibility are calculated, based on the aforementioned results in conjunction with the cumulative damage theory for linear fatigue. The histograms that depict the fatigue loads caused by thrust forces at the blade root and tower base, and bending moment at the tower base, are displayed in Fig. 25. An examination reveals that the equivalent fatigue loads under uniform inflow condition are notably smaller than those under turbulent winds, owing to the relatively low amplitude of the aerodynamic loads. Under uniform winds, the equivalent fatigue loads maintain the same values which reveals that the effects of blade and tower flexibility can be negligible. Additionally, it is noted that the equivalent fatigue loads caused by thrust forces at the blade root and tower base, as well as those induced by the bending moments under turbulent inflow conditions, are approximately 2–3 times, 1.5–2.5 times, and 1.5–2.5 times larger than

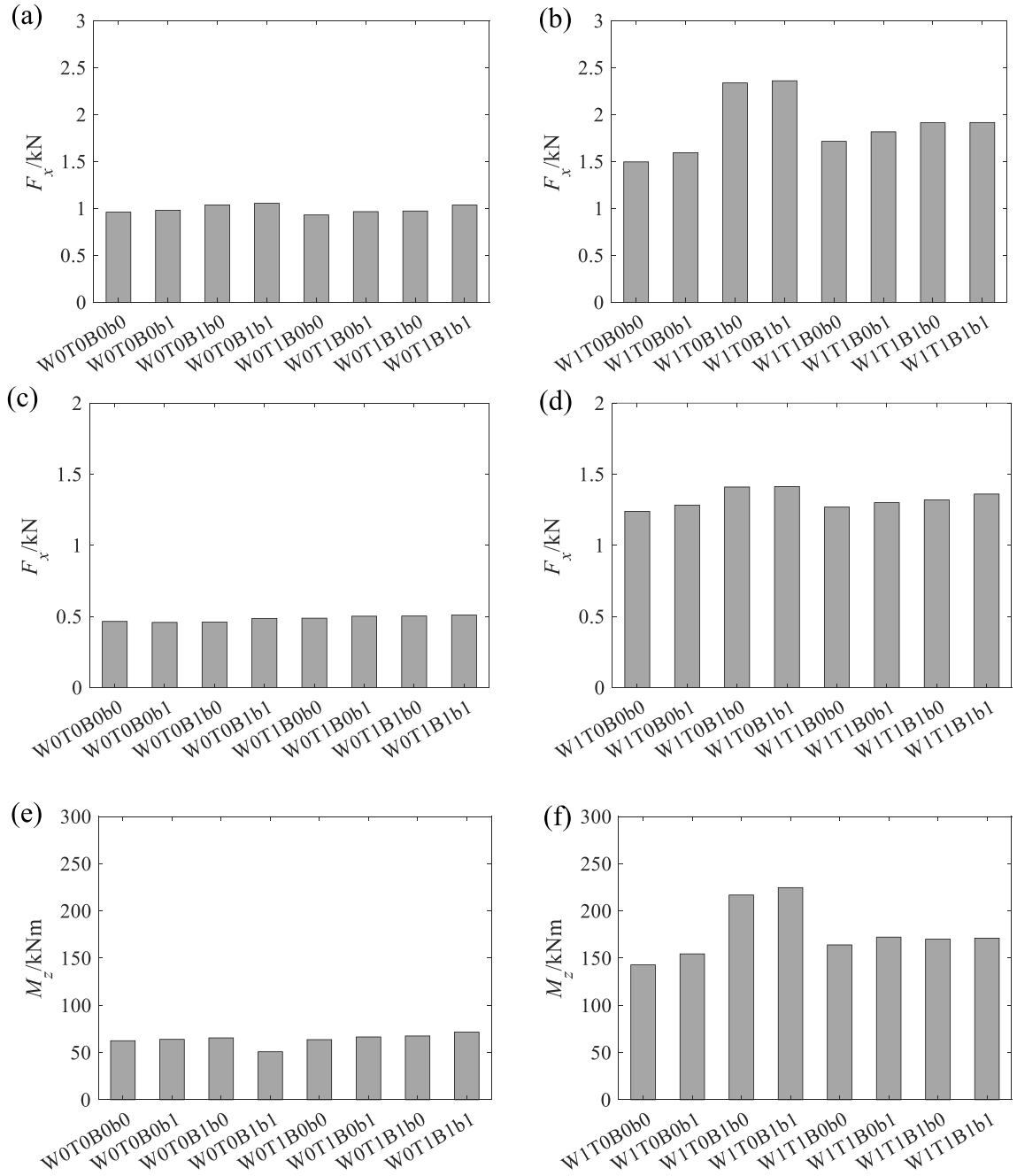


Fig. 25. Equivalent fatigue loads of: (a) the thrust force at the blade root under uniform and; (b) turbulent winds; (c) the thrust force at the tower base under uniform and; (d) turbulent winds; (e) the bending moment at the tower base under uniform and; (f) turbulent winds.

those under uniform inflow conditions. Moreover, the equivalent fatigue load increase ranges around 4 times when comparing the fully flexible case with the fully rigid case. Therefore, the findings underscore the significance of carefully considering wind flow conditions and component flexibility when designing and maintaining wind turbines structures.

In the context of turbulent inflow conditions, a comparative study of various cases is conducted to assess the impact of blade and tower motions on the equivalent fatigue loads. Results show that blade motions in the flap-wise direction have significant effect on the equivalent fatigue loads on both the blade root and the tower base. It is found that the equivalent fatigue loads calculated by the thrust force and bending moment on the tower base are approximately 1.6 times and 1.4 times higher than the fully rigid case when only considering the flap-wise motions of the blades. It is observed that the motion of tower has a weakening effect on the equivalent fatigue loads. Specifically, when considering both the motions of the tower and the flap-wise motions of blades, the equivalent fatigue loads are reduced by approximately 27% and 25%, respectively, based on the calculated thrust force and bending moment on the tower base.

4.3. Aeroelastic responses of wind turbine

4.3.1. Displacements at blade tip

Fig. 26 illustrate the time series of displacements at the blade tip under uniform and turbulent inflow conditions, respectively. To facilitate comparison, only a 25 s data are presented, specifically, the time range of 160–185 s under uniform inflow conditions and 210–235 s

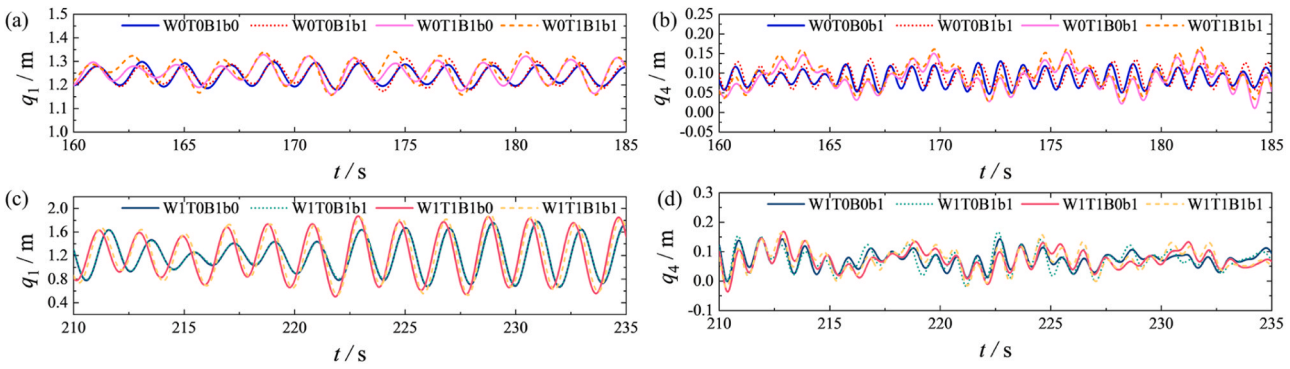


Fig. 26. Time series of: (a) the flap-wise and; (b) edgewise displacements at the blade tip under uniform winds; (c) the flap-wise and; (d) edgewise displacements at the blade tip under turbulent winds.

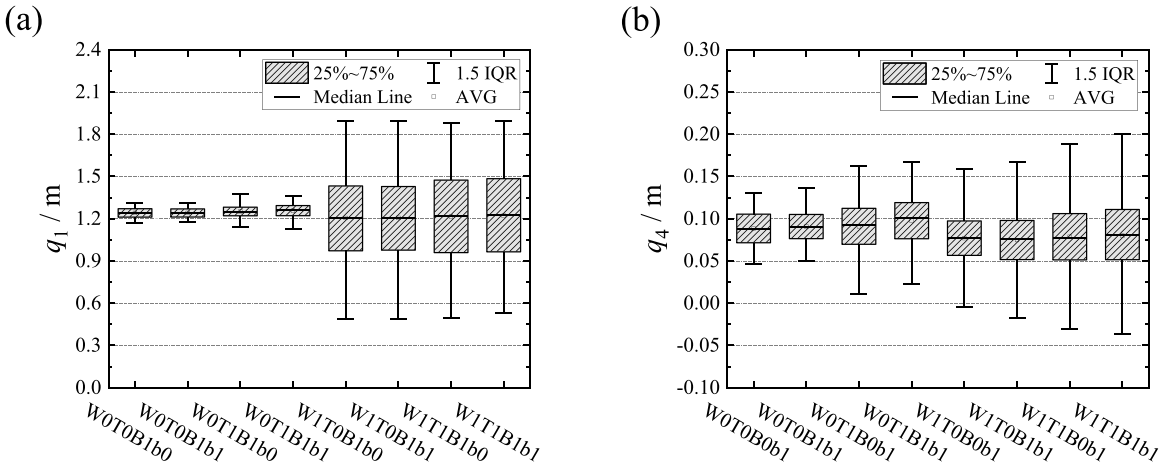


Fig. 27. Box plots of the: (a) flap-wise and; (b) edgewise displacements at the blade tip.

under turbulent inflow conditions. In Fig. 26, a comparison of the time series of displacements at the blade tip under different inflow conditions indicates that the amplitude of the flap-wise displacement is within 0.1–0.15 m, while the amplitude of the edgewise displacement is within 0.05–0.07 m in uniform winds. The amplitude of the flap-wise displacement is in the range of 1.0–1.2 m, and the edgewise displacement amplitude is in the range of 0.05–0.15 m under turbulent inflow conditions. The significant increase in the blade tip vibration amplitude under turbulent inflow conditions is primarily attributed to the fluctuating wind speed, which leads to load fluctuation on the blade. Such fluctuations are negligible under uniform inflow conditions.

Furthermore, it is observed that the motion of the tower, under the same wind conditions, has a noticeable impact on the flap-wise displacement at the blade tip. Conversely, the edgewise motions of blades have a relatively minor influence on the flap-wise displacement. Consequently, the time series of flap-wise displacement at the blade tip for W0T0B1b0 and W0T0B1b1, as well as W0T1B1b0 and W0T1B1b1 exhibit similar trends. Specifically, under uniform inflow conditions, the motion of the tower results in a larger sinusoidal curve adding to the edgewise displacement at the blade tip, while flap-wise motions of blades have a comparatively smaller effect. Similarly, under turbulent inflow conditions, the four curves show similar changes, with the effect of tower motion on the flap-wise displacement being more pronounced than the effect of blade motions in the edgewise direction.

To analyze the statistical properties of the displacement data, a box plot of the time series data at the blade tip in two directions is presented in Fig. 27. As shown in Fig. 27(a), the IQR, maximum and minimum values of the flap-wise displacement at the blade tip are significantly larger under turbulent wind conditions than those under uniform wind conditions, which is primarily attributed to the fluctuation of wind speed. The average and median values of displacement in turbulent winds are smaller than those in uniform winds owing to the vertical distribution of the wind speed. The turbulent wind is generated by the spire in the numerical wind tunnel, and the vertical distribution of the averaged wind velocity increases with height, indicating that the average wind speed is greater at higher altitudes. In contrast, the averaged wind speed is similar under uniform inflow conditions. Consequently, the average aerodynamic loads and displacements under uniform winds are higher than those in turbulent winds. These values vary slightly, and the differences can be negligible for cases in the same inflow conditions. Furthermore, as illustrated in Fig. 27(b), it is noticeable that the wind conditions exert a comparatively minor effect on the statistical data at the blade tip in the edgewise direction compared to that in the flap-wise direction. This is due to the fact that the displacement in the edgewise direction is predominantly influenced by the tangential force exerted on the blade, and the magnitude of the tangential force is chiefly determined by the rotational speed. In addition, the motion of the tower has a greater impact on the IQR, maximum and minimum values of displacement, while the motions of the blades in the edgewise direction has minimal impact. Both the flap-wise motions of blades and the motions of the tower contribute to the IQR and the average displacement at the blade tip in the edgewise direction. Regarding the edgewise displacement at the blade tip, fully flexible cases obtain the maximum values, including the median, average, the IQR, maximum and minimum values, in the same inflow conditions.

The power spectrum density (PSD) plots, depicting the displacements at the blade tip across various scenarios, have been presented in Fig. 28. It becomes evident that the principal frequencies of structural

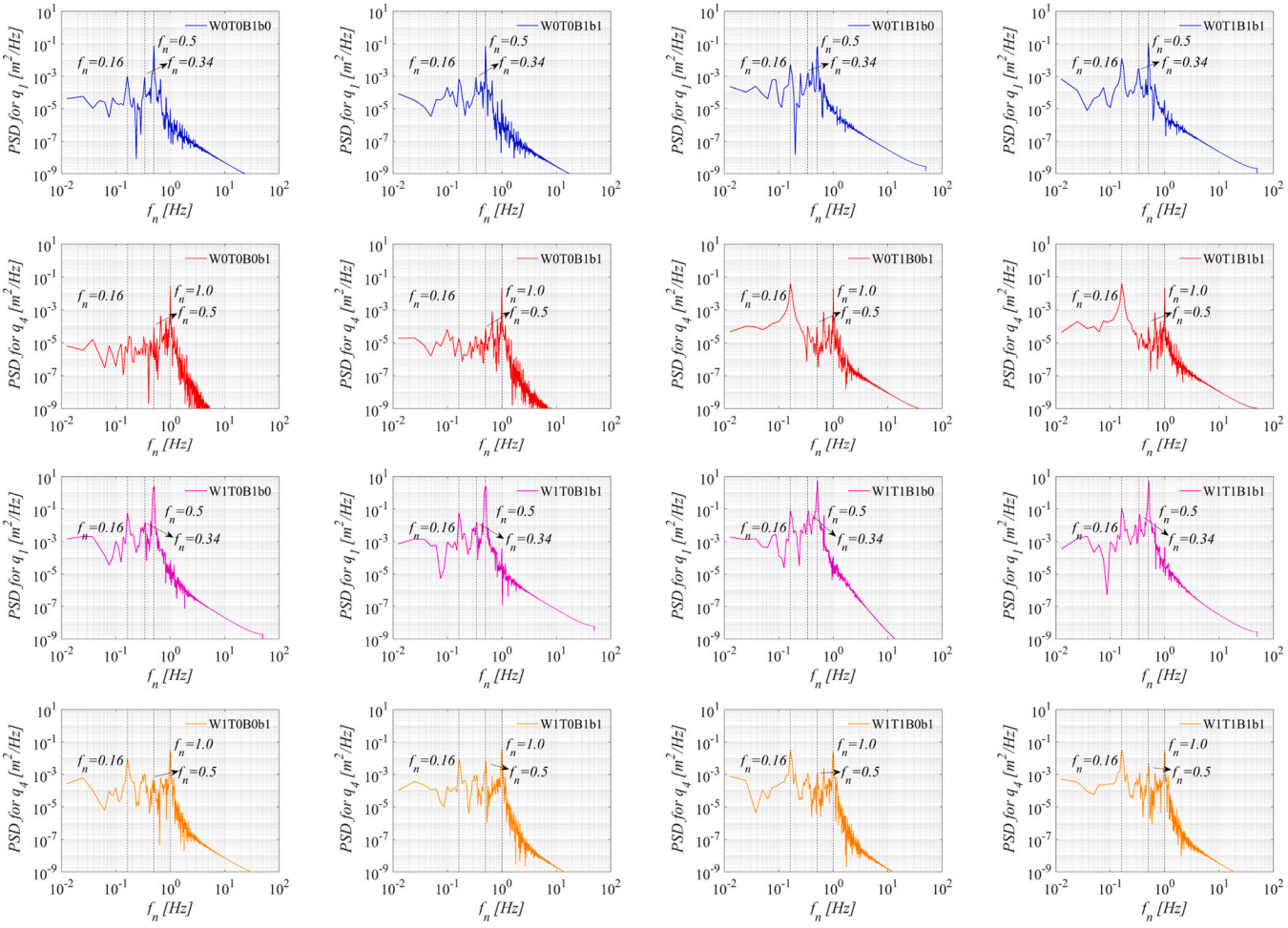


Fig. 28. PSD of the displacement at the blade tip considering different blade and tower flexibilities under uniform inflow condition.

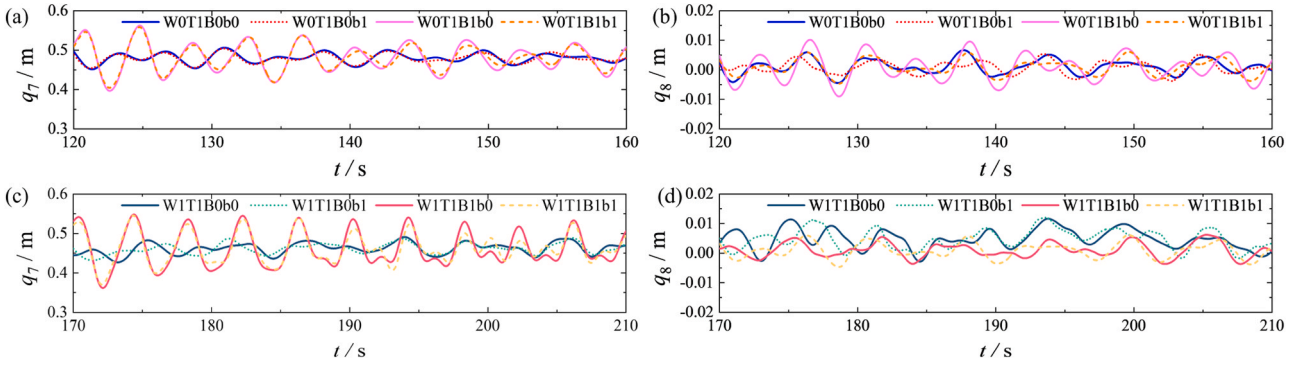


Fig. 29. Time series of: (a) the fore-aft and; (b) side-side displacements at the tower top under uniform winds; (c) the fore-aft and; (d) side-side displacements at the tower top under turbulent winds.

response are intricately linked to the rotations of the three blades. The two frequencies associated with flap-wise displacements at the blade tip, namely 0.16 Hz and 0.5 Hz, can be observed obviously for all cases. Furthermore, the primary frequency of blade vibration in the flap-wise orientation is ascertained at 0.34 Hz, while the corresponding frequency for blade motion in the edgewise direction is noted at 1 Hz. Concurrently, the secondary frequency of blade vibration in the flap-wise direction approximates 0.66 Hz and it can be observed only if the tower flexibility is considered which implies the necessity of the two-way FSI simulation for aeroelastic response analysis of wind turbine.

4.3.2. *Displacements at tower top*

Fig. 29 present the time series of displacement at the tower top under different inflow conditions. Since the tower exhibits lower frequency vibration than the blade, the statistical data with 40 s are provided, i.e., 120–160 s data for uniform winds and 170–210 s for turbulent winds. The results show that the fore-aft displacement at the tower top is obviously larger than the side-side displacement under either uniform or turbulent inflow conditions. The displacement in the side-side direction under either uniform or turbulent inflow conditions appears to be chaotic and the effect of blade and tower flexibility is not apparent. However, the flap-wise motions of blades have a greater impact on the

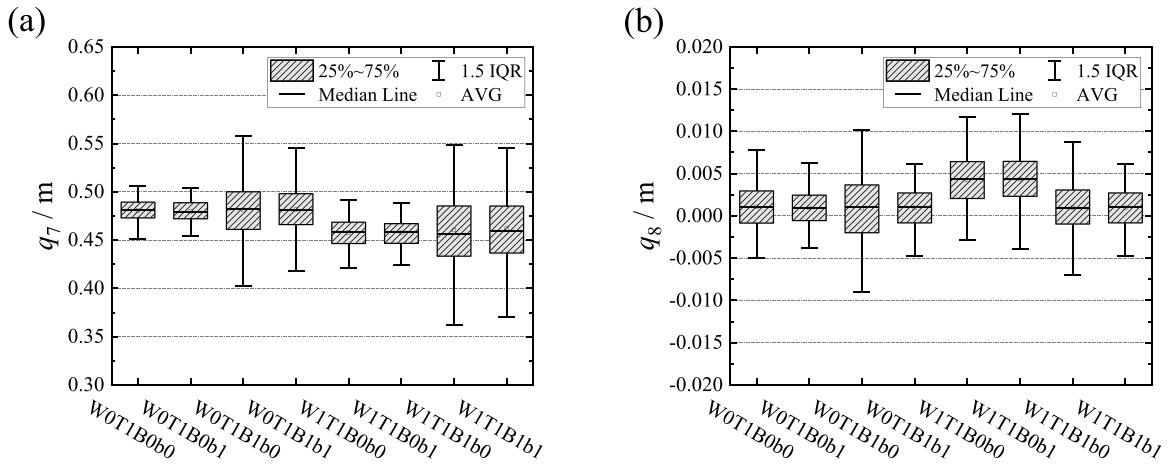


Fig. 30. Box plots of the: (a) fore-aft and; (b) side-side displacements at the tower top.

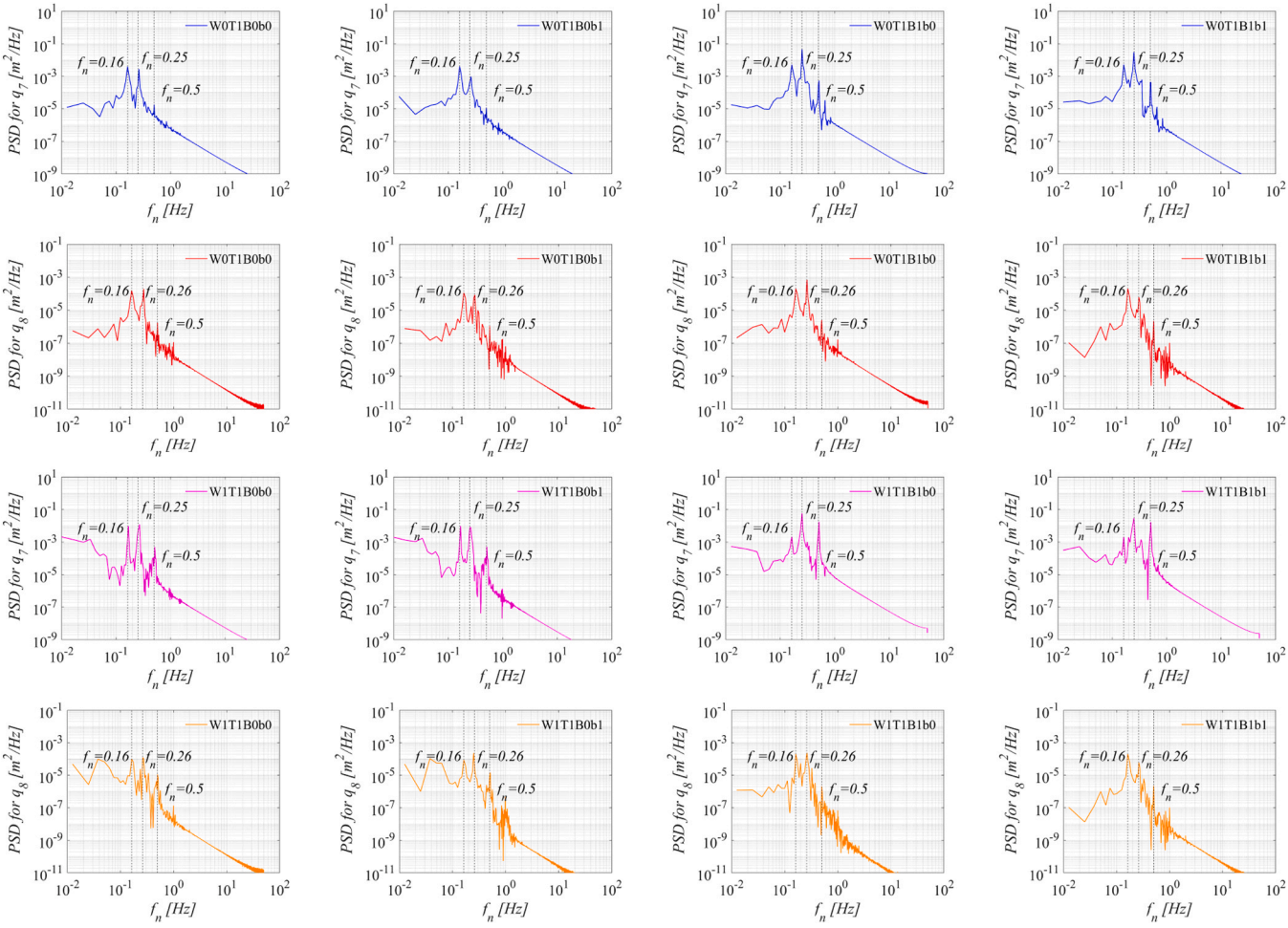


Fig. 31. PSD of the displacement at the tower top considering different blade and tower flexibilities under uniform inflow condition.

fore-aft displacement at the tower top than the edgewise motions of blades under different inflow conditions. There is some overlap between cases due to the negligible effect of edgewise motions of blades, such as W0T1B0b0 and W0T1B0b1, as well as W0T1B1b0 and W0T1B1b1 in Fig. 29(a), W1T1B0b0 and W1T1B0b1, as well as W1T1B1b0 and W1T1B1b1 in Fig. 29(c).

Fig. 30 presents the box plots of the fore-aft and side-side displacements at the tower top. As evident from the data, the average and median values of fore-aft displacement are lower under turbulent wind conditions than those in uniform wind conditions, owing to the vertical variation of wind speed. Remarkably, compared with the cases in uniform winds, turbulent wind conditions result in a wider IQR of displacement, with the same blade flexibility, suggesting increased data dispersion and displacement amplitude amplification. Fig. 30 demonstrates that both tower motion and blade flap-wise motion lead to larger IQR and ranges of fore-aft displacement which means that the vibration

amplitude of displacement at the tower top under turbulent winds are much higher for these cases. It also reveals that the proper choice of the DoFs of the wind turbine structural model to accurately calculate the aeroelastic response. Regarding the side-side displacement, there is no obvious variations due to the limited amplitude in Fig. 30(b).

The PSD profiles delineating displacements at the tower top across different cases are presented in Fig. 31. Evidently, the rotations of the three blades impart pronounced vibrations at the tower top, characterized by frequencies of 0.16 Hz and 0.5 Hz which are similar to the displacements at the blade tip. Concurrently, the tower exhibits a natural vibration frequency of approximately 0.26 Hz, regardless of whether the motion occurs in the fore-aft or side-side directions. Furthermore, it is noteworthy that the first frequency of blade vibration in the flap-wise direction (0.34 Hz) is also discernible in either the fore-aft or side-side displacement recorded at the tower top under turbulent wind conditions, particularly in the case denoted as W1T1B1b1. This observation underscores the imperative necessity of two-way FSI simulations for wind turbine analyses, accentuating their role in comprehensively capturing these vibrational phenomena.

5. Conclusions and future works

In this paper, we present a novel framework that allows for the integration of LES turbulent model and a structural dynamic model to carry out the two-way FSI analysis for wind turbines to investigate aerodynamic loads and aeroelastic responses considering different inflow conditions, and blade and tower flexibility. The following conclusions are drawn:

1. The periodicity of thrust forces on both blade root and tower base is evident while that of the bending moment at the tower base is less obvious under the uniform inflow conditions. However, the periodicity of all aerodynamic loads under turbulent inflow conditions is not apparent due to the fluctuations of inflow winds.
2. The aerodynamic loads are significantly influenced by blade and tower flexibility under uniform inflow conditions, especially by flap-wise motions of blades. Effects of turbulence on aerodynamic loads result in increased fluctuations, with flap-wise motions of the blades found to be more critical to load magnitude compared to edgewise motions. The inclusion of tower motion mitigates this aerodynamic load to some extent through coupling effects.
3. It is noted that the equivalent fatigue loads induced by turbulent winds are significantly larger than those under uniform inflow conditions. Moreover, the equivalent fatigue loads calculated by the thrust force and bending moment at the tower base when only considering the flap-wise motions of the blades, are found to be approximately 1.6 times and 1.4 times higher than the fully rigid case. The motion of the tower is observed to have a weakening effect on the equivalent fatigue loads. Specifically, when accounting for both the tower motion and flap-wise motions of blades, the equivalent fatigue loads are reduced by approximately 27% and 25%, respectively, based on the calculated thrust force and bending moment at the tower base.
4. The vibration amplitude at the blade tip under turbulent winds is much larger than that in uniform winds, primarily attributed to the fluctuating wind speed which leads to load fluctuation on the blade. Under the same wind conditions, it is observed that the motion of the tower has a noticeable impact on the flap-wise displacement at the blade tip. Conversely, the edgewise motions of the blades exhibit relatively minor influence on the flap-wise displacement.
5. The fore-aft displacement at the tower top is obviously larger than the side-side displacement under different wind conditions. The side-side displacement under different inflow conditions appears to be chaotic and the effect of blade and tower flexibility is not apparent. However, the flap-wise motions of blades have a greater impact on the fore-aft displacement at the tower top than the edgewise motion of blade under different inflow conditions.

The advancement of the two-way FSI simulation methodology remains an ongoing endeavor, with several aspects warranting further exploration in the future:

1. Enhanced simulation precision: Efforts to refine the accuracy of the simulation approach will persist. Notably, forthcoming investigations will encompass the realistic wind turbine models, featuring three-dimensional rotating blades with pre-bending. Additionally, there will be a concerted emphasis on the employment of more precise deformation theories, particularly those based on geometrically accurate beam models as the blade length extends.
2. Validation and comparative analyses: A pivotal phase of future work will entail the validation of the two-way FSI simulations through field tests and conduct the comparative evaluations across diverse simulation methodologies, including the proposed two-way FSI simulation, Bladed, NREL OpenFAST, and HAWC2.
3. Reduction of computational costs: A thorough assessment will be undertaken to evaluate the practical applicability of both one-way and two-way FSI simulations concerning wind turbine aerodynamics and dynamics. This inquiry seeks to discern how these approaches can potentially optimize computational resources and reduce associated costs.

CRediT authorship contribution statement

Zhang Dongqin: Software, Visualization, Writing – original draft, Writing – review & editing. **Li Weipeng:** Formal analysis, Investigation, Software, Visualization. **Liu Zhenqing:** Conceptualization, Funding acquisition, Methodology, Resources, Supervision, Writing – review & editing. **Hu Gang:** Methodology, Writing – review & editing. **Cheng Ling:** Supervision, Writing – review & editing. **Zhang Jize:** Methodology, Writing – review & editing.

Declaration of Competing Interest

The authors declare that they have no known competing financial interests or personal relationships that could have appeared to influence the work reported in this paper.

Data Availability

The authors do not have permission to share data.

Acknowledgements

This study was supported by National Natural Science Foundation of China (51978307).

References

[1] GWEC. Global wind report 2022. 2022.
[2] Hansen MOL, Sørensen JN, Voutsinas S, Sørensen N, Madsen HAa. State of the art in wind turbine aerodynamics and aeroelasticity. Prog Aerosp Sci 2006;42:285–330.
[3] Martin H.O. Aerodynamics of wind turbines. 2nd ed. In: Earthscan in the UK and USA: 2008.
[4] Luo K, Zhang S, Gao Z, Wang J, Zhang L, Yuan R, et al. Large-eddy simulation and wind-tunnel measurement of aerodynamics and aeroacoustics of a horizontal-axis wind turbine. Renew Energy 2015;77:351–62.
[5] Leishman JG. Challenges in modelling the unsteady aerodynamics of wind turbines. Wind Energy 2002;5:85–132.
[6] Dai JC, Hu YP, Liu DS, Long X. Aerodynamic loads calculation and analysis for large scale wind turbine based on combining BEM modified theory with dynamic stall model. Renew Energy 2011;36:1095–104.
[7] Vaz JRP, Pinho JT, Mesquita ALA. An extension of BEM method applied to horizontal-axis wind turbine design. Renew Energy 2011;36:1734–40.

[8] Sun Z, Chen J, Shen WZ, Zhu WJ. Improved blade element momentum theory for wind turbine aerodynamic computations. Renew Energy 2016;96:824–31.
[9] Sørensen JN, van Kuik GAM. General momentum theory for wind turbines at low tip speed ratios. Wind Energy 2011;14:821–39.
[10] Giahi MH, Jafarian Dehkordi A. Investigating the influence of dimensional scaling on aerodynamic characteristics of wind turbine using CFD simulation. Renew Energy 2016;97:162–8.
[11] Cai X, Gu R, Pan P, Zhu J. Unsteady aerodynamics simulation of a full-scale horizontal axis wind turbine using CFD methodology. Energy Convers Manag 2016;112:146–56.
[12] Bangga G, Lutz T. Aerodynamic modeling of wind turbine loads exposed to turbulent inflow and validation with experimental data. Energy 2021;223:120076.
[13] Lee M-H, Shiah YC, Bai C-J. Experiments and numerical simulations of the rotor-blade performance for a small-scale horizontal axis wind turbine. J Wind Eng Ind Aerodyn 2016;149:17–29.
[14] Alkhabbaz A, Yang H-S, Tongphong W, Lee Y-H. Impact of compact diffuser shroud on wind turbine aerodynamic performance: CFD and experimental investigations. Int J Mech Sci 2022;216:106978.
[15] Malcolm D., Laird D. Modeling of blades as equivalent beams for aeroelastic analysis. 41st Aerospace Sciences Meeting and Exhibit, American Institute of Aeronautics and Astronautics; n.d. ⟨https://doi.org/10.2514/6.2003–870⟩.
[16] Liu Z, Wang Y, Nyangi P, Zhu Z, Hua X. Proposal of a novel GPU-accelerated lifetime optimization method for onshore wind turbine dampers under real wind distribution. Renew Energy 2021;168:516–43.
[17] Rajamohan S, Vinod A, Pragada Venkata Sesha Aditya M, Gopalakrishnan Vadivudaiyanayaki H, Nhanh Nguyen V, Arıcı M, et al. Approaches in performance and structural analysis of wind turbines – a review. Sustain Energy Technol Assess 2022;53:102570.
[18] Leng J, Gao Z, Wu MCH, Guo T, Li Y. A fluid–structure interaction model for large wind turbines based on flexible multibody dynamics and actuator line method. J Fluids Struct 2023;118:103857.
[19] ElliotT A.S., Wright A.D. ADAMS/WT: an industry-specific interactive modelling interface for wind turbine analysis. vol. 01/23–26/94, New Orleans, La, USA,: 1994, p. 111–22.
[20] Dassault Systems. SIMPACK 2017.1 Simpack Assistant. 2017.
[21] Lindenburg C. Phatas user's manual WMC. Wieringerwerf, the Netherlands: 2018.
[22] Øye S. FLEX 5 user manual. Danske Techniske Hogskole: 1999.
[23] Bossanyi E. GH Bladed theory manual. GH & Partners Ltd,; 2003.
[24] Larsen TJ, Hansen AM. How 2 HAWC2, the User's Manual, Tech. Rep. Risø-R1597. Roskilde and Kgs. Lyngby, Denmark: Risø National Laboratory, Technical University of Denmark,; 2007.
[25] Couturier PJ, Skjoldan PF. Implementation of an advanced beam model in BHawC. J Phys: Conf Ser 2018;1037:062015.
[26] NREL. Openfast. ⟨https://github.com/OpenFAST/openfast⟩ 2020.
[27] Carrión M, Steijl R, Woodgate M, Barakos GN, Munduate X, Gomez-Iradi S. Aeroelastic analysis of wind turbines using a tightly coupled CFD–CSD method. J Fluids Struct 2014;50:392–415.
[28] Yu DO, Kwon OJ. Predicting wind turbine blade loads and aeroelastic response using a coupled CFD–CSD method. Renew Energy 2014;70:184–96.
[29] Della Posta G, Leonardi S, Bernardini M. A two-way coupling method for the study of aeroelastic effects in large wind turbines. Renew Energy 2022;190:971–92.
[30] Dose B, Rahimi H, Herráez I, Stoevesandt B, Peinke J. Fluid-structure coupled computations of the NREL 5 MW wind turbine by means of CFD. Renew Energy 2018;129:591–605.
[31] Sayed M, Lutz Th, Krämer E, Shayegan Sh, Wüchner R. Aeroelastic analysis of 10 MW wind turbine using CFD–CSD explicit FSI-coupling approach. J Fluids Struct 2019;87:354–77.
[32] Chen C, Duffour P, Fromme P, Shen X, Hua X, Chen Z. Simplified complex-valued modal model for operating wind turbines through aerodynamic decoupling and multi-blade coordinate transformation. J Sound Vib 2023;547:117512.
[33] Yassen YElS, Abdelhameed AS, Elshorbagy KA. An examination of hub wind turbine utilizing fluid-structure interaction strategy. Alex Eng J 2023;64:1–11.
[34] Cai Y, Zhao H, Li X, Liu Y. Effects of yawed inflow and blade-tower interaction on the aerodynamic and wake characteristics of a horizontal-axis wind turbine. Energy 2023;264:126246.
[35] Ji B, Zhong K, Xiong Q, Qiu P, Zhang X, Wang L. CFD simulations of aerodynamic characteristics for the three-blade NREL Phase VI wind turbine model. Energy 2022;249:123670.
[36] Sabale AK, Gopal NKV. Nonlinear aeroelastic analysis of large wind turbines under turbulent wind conditions. AIAA J 2019;57:4416–32.
[37] Zhou Y, Xiao Q, Liu Y, Incecik A, Peyrard C, Wan D, et al. Exploring inflow wind condition on floating offshore wind turbine aerodynamic characterisation and platform motion prediction using blade resolved CFD simulation. Renew Energy 2022;182:1060–79.
[38] Li Q, Murata J, Endo M, Maeda T, Kamada Y. Experimental and numerical investigation of the effect of turbulent inflow on a Horizontal Axis Wind Turbine (Part I: Power performance). Energy 2016;113:713–22.
[39] Li Y, Castro AM, Sinokrot T, Prescott W, Carrica PM. Coupled multi-body dynamics and CFD for wind turbine simulation including explicit wind turbulence. Renew Energy 2015;76:338–61.
[40] Ishihara T., Yamaguchi A., Fujino Y. Development of a new wake model based on a wind tunnel experiment. Global Wind Power 2004.
[41] Ansys Inc. Fluent theory guide. Canonsburg, PA 2022.